Comput Mech (2005) 35: 237–264
DOI 10.1007/s00466-004-0575-z

ORIGINAL PAPER

D. Ehrlich · F. Armero

Finite element methods for the analysis of softening plastic hinges in beams and frames

Received: 11 August 2003 / Accepted: 16 March 2004 / Published online: 2 December 2004
© Springer-Verlag 2004

Abstract This paper presents new finite element methods for the analysis of localized failures in plastic beams and frames in the form of plastic hinges. The hinges are modeled as discontinuities of the generalized displacements of the underlying Timoshenko beam/rod theory. Hinges accounting for a discontinuity in the transversal and longitudinal displacements and the rotation field are developed in this context. A multi-scale framework is considered in the incorporation of the dissipative effects of these discontinuities in the large-scale problem of a beam and a general frame. A localized softening cohesive law relating these generalized displacements with the stress resultants acting at the level of the cross section is effectively introduced in the frame response. The resulting models, referred to as localized models, are then able to capture the localized dissipation observed in the localized failures of these structural members, avoiding altogether the inconsistencies observed for classical models in the stress resultants with strain softening. The constructive approach followed in the development of these models leads naturally to the formulation of enhanced strain finite elements for their numerical approximation. In this context, we develop new finite elements incorporating the singular strains associated to the plastic hinges at the element level. A careful analysis is presented so the resulting finite elements avoid the phenomenon of stress locking, that is, an overstiff response in the softening of the hinge, not allowing for the full release of the stress. The accurate approximation of the kinematics of the hinges requires a strain enhancement linking the jumps in the deflection and the rotation fields, given the coupled definition of the transverse shear strain in these two fields. Different enhanced strain elements, involving different base finite elements and different enhancement strategies, are considered and analyzed in detail. Their performance are then compared in several representative numerical simulations. These analyses identify optimally enhanced finite elements for the accurate modeling the localized failures observed in common framed structures.

Keywords Beams and frames · Plastic hinge · Strong discontinuity · Enhanced finite elements · Stress locking

D. Ehrlich · F. Armero (✉)
Structural Engineering, Mechanics and Materials Department of Civil and Environmental Engineering University of California, Berkeley CA 94720, USA
E-mail: armero@ce.berkley.edu

1 Introduction

The analysis of the failure of structural systems is one of the main problems in basically any practical application in structural engineering. Of particular interest is the understanding of the observed localized failures in which the columns and beams of framed structures fail in concentrated zones, usually described as plastic hinges. The study of the post-failure response, with the structure exhibiting a reduction in the load capacity for additional deformation (generically referred to as softening), appears as a clear challenge given the nonlinearity of the resulting inelastic problem. The development of numerical techniques for the accurate resolution of these solutions appears then as a clear choice. The goal of this paper is precisely the formulation of accurate and efficient finite element methods for the analysis and numerical simulation of plastic hinges in beams and frames, to model their softening post-limit response.

Initial attempts in the analysis of typical structural members considered classical theories, like the Timoshenko beam theory, in combination with standard plasticity models in stress resultant form. To model the overall softening response of the structure, a strain softening law can be considered at the constitutive or cross-section level, e.g., between the bending moment and curvature (see Darvall [1984], and Bazant et al. [1987]). However, strain softening is known to lead to serious inconsistencies in inelastic models of the local continuum. The mathematical problem becomes ill-posed, and the solutions obtained with them are

physically meaningless. A typical situation is the inadequacy of a plastic model with strain softening law to model the failure of a rod in the fully dynamic case involving wave propagation, as presented in Bažant & Belytschko [1985]. The finite element solutions of the problem show the typical pathological mesh size dependence in the conditions; see again Bažant et al. [1987] for an example in the structural context of interest here. In fact, the numerical methods are just obtaining the non-physical solutions associated to the continuum models with strain softening as the mesh is refined.

These inconsistencies can all be traced back to the lack of a characteristic length defining a finite zone where the dissipative softening effects are to localize in the continuum problem. Remarkably, the mathematical analyses presented in Armero & Ehrlich [2002] identify the same difficulties in inelastic models of a Timoshenko beam/rod with strain softening despite the existence of a well-defined length scale in these models: namely, the thickness of the structural member. A complete linearized spectral analysis of the governing equations has been presented in this reference identifying the ill-posedness of the mathematical problem with a strain softening law (that is, a relation between the generalized strain measures and the conjugate stress resultants defining the Timoshenko theory of a beam/rod). The significance of this result has been illustrated with the exact closed-form solution of the wave propagation in a simply supported beam with strain softening (i.e. moment versus curvature softening law), extending in this way the results presented originally in Bažant & Belytschko [1985] for a rod. This solution shows again to be physically incorrect, with the model unable to capture the localized dissipation associated to the formation of the plastic hinges.

These results motivate the consideration of the so-called strong discontinuity approach in the modeling and numerical resolution of these localized solutions. The plastic hinges are then understood as discontinuities of the generalized displacement fields defining the underlying structural theory under consideration. This includes discontinuities in the longitudinal and transversal displacements of the beam/rod middle-axis, and the rotation of the beam cross-section. In this way, we can model general responses of the plastic hinges (for example, bending moment versus relative rotation, or coupled transverse shear force and bending moment versus relative rotation and deflection jump). This situation is to be contrasted with formulations incorporating a plastic hinge modeled with a zone of finite length where the strain softening takes place; see e.g. Darvall [1984], Bažant et al. [1987] or the review in Bažant & Cedolin [1991] (Sect. 13.6).

The strong discontinuity approach can be found developed in the recent literature. Early works include Simo et al. [1993], Larsson et al. [1993], Armero & Garikipati [1995, 96], and Oliver [1996a, b], among others. We presented in Armero[1999] and Armero[2001] a multi-scale formulation of this approach. In this way, the strong discontinuities are seen as tools for the incorporation of the localized dissipative effects observed in the failures of interest in the large-scale problem of the original continuum. This approach leads to what we refer to as localized models, which incorporate these effects without the need to introduce explicitly the small scales associated to the failure of the material. Furthermore, the constructive way in formulating these models, with the strong discontinuities (or, rather, the singular strain fields associated to these solutions) being introduced locally in a small neighborhood of the material points that eventually vanishes, leads naturally to the formulation of enhanced strain finite element methods for their numerical approximation. The interpolated strain fields of a base element are enhanced, locally at the element level, with the singular fields associated to the strong discontinuities. No regularization of the strong discontinuities is required in these formulations, with the final finite elements incorporating the localized dissipative effects objectively.

We have developed recently in Armero & Ehrlich [2002] this multi-scale framework for the modeling of plastic hinges in beams and rods, arriving to localized models in these contexts. The mathematical analyses presented in this reference show that the resulting initial boundary-value problems recover their mathematical well-posedness and their physical significance. In particular, these properties were verified after obtaining the exact closed-form solution of the wave propagation in a simply supported beam with a softening hinge (i.e. moment versus rotation softening law) at its center. It is the particular goal of the present paper to use this framework for the development of new enhanced strain finite element methods for the numerical resolution of these discontinuous solutions. The consideration of beam finite elements incorporating plastic hinges can be found in Darval & Mendis [1984], King et al. [1992], and Jirásek [1997], among others. This includes the case of plastic hinges regularized by a zone of finite length where the softening response takes place, as considered in the first of these references. The strong discontinuity approach proposed here allows for a rigorous and systematic development of these finite element methods, as illustrated by the considerations in this paper.

Crucial to the accurate modeling of the strong discontinuities by the finite elements is the avoidance of the so-called stress locking. This situation is typical in the original smeared crack models of concrete (see e.g. Rots et al. [1985]), and it involves an overstiff response of the numerical model when trying to capture the softening of a discontinuity (crack or similar). A spurious transfer of stress may occur across the discontinuity, not allowing the full release of the stress in the fully softened discontinuity. This situation may even lead to a hardening rather than a softening overall response of the solid or structure. Finite element formulations based on the strong discontinuity approach, carefully accounting for the kinematics of the strong discontinuities and the equilibrium conditions across them, have been shown to

avoid stress locking. We refer to Jirásek [2000] for complete details on these arguments.

We present in this paper a complete analysis of these considerations in the context of plastic hinges in beams and rods. The final goal is again to obtain new finite elements that incorporate these plastic hinges in their local interpolations. The coupling between the deflection and rotation fields in the definition of the transverse shear strain of a Timoshenko beam leads to a different problem when compared with the plane or three-dimensional continuum. The more involved kinematics require the formulation of new and more involved enhancements of the element strains to capture correctly the kinematics of the plastic hinges. It is precisely the avoidance of the stress locking as defined above that is proposed here as a general methodology for the design of these enhanced finite elements. More specifically, the requirement that the finite element should accommodate a fully softened plastic hinge with no strains (or stress resultants) is shown to define these enhancements of the strains. Enhancements involving linked contributions of the deflections and rotation discontinuity jumps are obtained in this way. We illustrate this approach for different base finite elements, from a simple two-noded piece-wise linear interpolation of the generalized displacements to the finite element presented in Crisfield [1984] involving a linked interpolation of the deflection and rotation fields. In all these cases, we arrive to local enhancements that avoid any stress locking and provide an accurate and efficient tool for the simulation of the localized failures of frame structures of interest here.

We limit the analyses in this paper to inelastic models of beams/rods expressed directly in stress resultants (e.g., bending moment, axial and transverse shear forces). In this context, the progression of the plastic effects through the beam cross section can be modeled with the appropriate hardening laws evolving the elastic domains in the stress resultant space; see the discussion in Lubliner [1990]. We refer also to this reference for details on how different factors, like the shape of the cross section, affect the models in stress resultants. We plan to extend these analyses in the future to the so-called fiber or layered models accounting for an explicit evaluation of these plastic effects through the beam thickness; see e.g. Bažant et al. [1987], Spacone et al. [1996a, b], and references therein. We emphasize again our specific interest in the modeling of the post-failure response rather than a simple evaluation of the limit loads of the structure as in classical limit analysis (see again the summary in Lubliner [1990] and references therein) or other related approaches, like the so-called quasi-hinge approach of Attalla et al. [1984], among others.

An outline of the rest of the paper is as follows. Section 2 presents the modeling of plastic hinges in beams and rods in the context of the aforementioned multi-scale framework. It defines, in this way, the mathematical problem for which we want to develop the finite element methods in the rest of the paper. The general framework of the enhanced strain finite element methods developed to this purpose is presented in Sect. 3. The discrete finite element equations are then identified. We left for Sect. 4 the design of the actual newly proposed finite elements. To this end, Sect. 4.1 describes in detail the phenomenon of stress locking in the context of the beam/rod theories of interest here, identifying the aforementioned general methodology for the successful design of the strain enhancements. This methodology is applied in Sect. 4.2 to 4.4 to different base finite elements arriving at a series of new enhanced strain finite elements that incorporate locally plastic hinges. Different analyses are presented, including eigenvalue analyses of the resulting stiffness matrices obtained after linearization, to obtain a complete understanding of the numerical properties of the different elements. For the same purpose, Sect. 5 presents a series of representative numerical simulations to illustrate and compare the numerical performance of the different finite elements. Section 6 presents a brief summary of the main findings and some additional concluding remarks. We finish with the short Appendix I, which includes some basic mathematical results on the approximations of the different functions required in the development of the new finite elements proposed in this paper.

2 Plastic hinges in beams and rods

We characterize in this section the plastic hinges observed in the localized failures in beams and rods within the context of strong discontinuities. More precisely, we make use of the multi-scale framework developed in Armero [1999] and Armero [2001] for the continuum to characterize these discontinuities in the generalized displacements defining a Timoshenko beam/rod.

The emphasis in the considerations to follow is then the efficient incorporation of the localized dissipative effects observed in these type of failures in the large-scale problem of such a beam, here understood as the problem exhibiting typical continuity requirements. This problem is briefly presented in Sect. 2.1. The incorporation of the strong discontinuities (or plastic hinges) is then carried out locally, through a local enhancement of the kinematics of the large-scale problem in Sect. 2.2. The consideration of this enhanced kinematics, with the inclusion of the generalized displacement jumps associated to the strong discontinuities, allows the characterization of the localized dissipative mechanisms of interest as elaborated in Sect. 2.3. These considerations lead then to the modeling of the small scales of the material response, being then introduced in the previous large-scale problem in Sect. 2.4.

2.1 The large scale problem

We are interested in the case of a straight beam/rod defined by its middle-axis $\mathscr{B} = (0, L) \subset \mathbb{R}$ for a length L

and the normal cross-section $\mathscr{A}(x)$ with $x \in \mathscr{B}$. For simplicity, and without loss of generality, we consider plane deformations of such a beam. Infinitesimal deformations are assumed in the general context of a Timoshenko beam theory, that is, with the cross-sections $\mathscr{A}$ remaining plane and undistorted but not necessarily orthogonal to the deformed axis. In this context, we consider the generalized displacements $\boldsymbol{u} := \{u, w, \vartheta\}$ corresponding to the longitudinal displacement $u(x)$ along the direction of the middle-axis, the transversal displacement $w(x)$, and the rotation $\vartheta(x)$ of the cross section, all functions of $x \in \mathscr{B}$. Figure 2.1 presents a sketch of this assumed kinematics including, in particular, the positive sign convention considered in what follows.

The strain measures of a classical Timoshenko beam/rod are then defined by

$$\boldsymbol{\varepsilon} = \boldsymbol{\varepsilon}(\boldsymbol{u}) := \{\varepsilon, \kappa, \gamma\} := \{\partial_x u, \partial_x \vartheta, \partial_x w - \vartheta\} \ , \tag{2.1}$$

for the axial strain ε, the bending strain κ and the transverse shear strain γ, all in terms of the generalized displacements $\boldsymbol{u}$ and their first derivatives $\partial_x(\cdot)$. Conjugate to these strain measures we have the stress resultants $\boldsymbol{\sigma} := \{N, M, V\}$ for the axial force N, the bending moment M and the transverse shear force V. Figure 2.1 depicts again the assumed positive sign convention for these quantities.

The quasi-static equilibrium for such a classical Timoshenko beam/rod is then characterized in weak form by the variational statement

$$\int_{\mathscr{B}} \boldsymbol{\sigma} \cdot \boldsymbol{\varepsilon}(\boldsymbol{\eta}) \mathrm{d}x = \int_{\mathscr{B}} \mathbf{f} \cdot \boldsymbol{\eta} \mathrm{d}x + \bar{\boldsymbol{\sigma}} \cdot \boldsymbol{\eta}\big|_{\partial_{\boldsymbol{\sigma}}\mathscr{B}} \qquad \forall \boldsymbol{\eta} \in \mathscr{V}_u \ , \tag{2.2}$$

for the distributed loads (forces and moments) per unit length $\mathbf{f} = \{n, m, p\}$, and imposed stress-resultants $\bar{\boldsymbol{\sigma}}$ on $\partial_{\boldsymbol{\sigma}}\mathscr{B} \subset \partial\mathscr{B}$, for the boundary $\partial\mathscr{B} = \{0, L\}$. The admissible variations η in (2.2) are defined by

$$\mathscr{V}_u = \{\boldsymbol{\eta} : \mathscr{B} \to \mathbb{R}^3 : \boldsymbol{\eta} \in H^1(\mathscr{B}) \text{ with } \boldsymbol{\eta} = 0 \text{ on } \partial_u\mathscr{B}\}, \tag{2.3}$$

for the part of the boundary $\partial_u\mathscr{B} \subset \partial\mathscr{B}$ with imposed generalized displacements ($\boldsymbol{u} = \bar{\boldsymbol{u}}$ on $\partial_u\mathscr{B}$). The usual assumption

$$\overline{\partial_u\mathscr{B} \cup \partial_{\boldsymbol{\sigma}}\mathscr{B}} = \partial\mathscr{B} \quad \text{and} \quad \partial_u\mathscr{B} \cap \partial_{\boldsymbol{\sigma}}\mathscr{B} = \emptyset, \tag{2.4}$$

is considered for each of the three components for a well-posed problem. Similarly, the definition of the admissible space of variations $\mathscr{V}_u$ in (2.3) considers the classical regularity assumption of functions with square integrable first derivative (i.e. $H^1(\mathscr{B})$ functions) characteristic, for example, of a linear elastic beam/rod. As we discuss below, the added effects associated to discontinuities of the generalized displacements $\boldsymbol{u}$, that is, the so-called strong discontinuities, are to be introduced separately. We refer to the problem defined by (2.2) to (2.3) as the large-scale problem.

Equation (2.2) corresponds to the principle of virtual work and leads, after a standard argument based on integration by parts, to the local equilibrium relations

$$\frac{\partial N}{\partial x} + n = 0, \qquad \frac{\partial V}{\partial x} + p = 0 \qquad \text{and} \qquad \frac{\partial M}{\partial x} + V + m = 0 \ . \tag{2.5}$$

We also recover the continuity of the stress resultants, that is, $[[\boldsymbol{\sigma}]] = 0$ for the jump $[[\cdot]]$ at any point $x \in \mathscr{B}$. It is important to observe the coupling (or "linking") between the bending moment and the transverse shear at this level, a direct consequence of the definition of the transverse shear strain γ in (2.1) linking the deflection w and the rotation ϑ fields. The coupling of the axial part of the problem can only occur in the assumed case of a straight infinitesimal beam at the constitutive level.

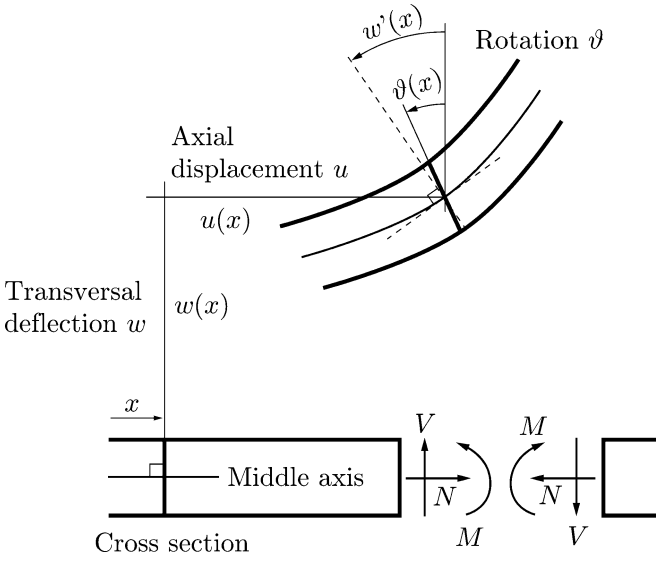

Fig. 2.1 Kinematics of a Timoshenko beam/rod in the infinitesimal range. The different quantities are shown according to the assumed positive sign convention

Remark 2.1. Continuum elastoplastic models. The above equations are to be supplemented with a constitutive relation. A plastic model can be easily formulated in stress resultant form through the relations

$$\left.\begin{aligned} &\boldsymbol{\sigma} = \partial_{\boldsymbol{\varepsilon}^e} W \quad \text{for} \quad \boldsymbol{\varepsilon}^e := \boldsymbol{\varepsilon} - \boldsymbol{\varepsilon}^p \quad \text{with} \\ &\dot{\boldsymbol{\varepsilon}}^p = \lambda \partial_{\boldsymbol{\sigma}} \phi, \quad \dot{\alpha} = \lambda \partial_q \phi, \\ &\phi \le 0, \quad \lambda \ge 0, \quad \lambda\phi = 0 \quad \text{and} \quad \lambda\dot{\phi} = 0 \ , \end{aligned}\right\} \tag{2.6}$$

for an elastic potential $W(\boldsymbol{\varepsilon}^e)$ in terms of the elastic part of the strain $\boldsymbol{\varepsilon}^e$, a yield function (or interaction diagram as it is usually known in this context) $\phi(\boldsymbol{\sigma}, q)$ in terms of the stress resultant $\boldsymbol{\sigma}$ and the hardening/softening internal variables q and α, for a general hardening/softening law $q(\alpha)$. Equations (2.6) have the same form as an associated plastic model in the local continuum, and so we shall refer to it as the "continuum model" in contrast with the "localized models" to be developed below.

2.2 The kinematics of strong discontinuities

The large-scale problem defined in the previous section assumes a generalized displacement field $\boldsymbol{u}$ and corresponding variations in the space $\mathscr{V}_u$ that satisfy the standard regularity conditions shown in (2.3). However, these conditions may be too restrictive for the characterization of the failure of the beam/rod. Of interest in this work is the modeling of the plastic hinges characteristic of the localized failures observed in structural members. It has been observed in Armero & Ehrlich [2002] that the direct use of a continuum model of the form (2.6) in combination with a strain softening law $q(\alpha)$ (i.e., with $H := -\partial_\alpha q < 0$) leads to the same inconsistencies as in the local continuum. This situation occurs even after the observation that a Timoshenko beam theory as considered above does possess a length scale in the model. For example, the ratio $r = \sqrt{\left(\partial^2_{\kappa\kappa} W\right)/\left(\partial^2_{\gamma\gamma} W\right)}$ can be readily shown to define such a length scale, being directly related to the thickness or height of the beam. The results presented in this reference show that this length scale is not sufficient to regularize the elastoplastic problem with strain softening, leading eventually to a mathematically ill-posed problem, physically meaningless.

In fact, by obtaining the closed-form solution of the fully nonlinear problem in particular cases, the appearance of discontinuities in the generalized displacement field $\boldsymbol{u}$ were observed. The associated strain measures involve then singular distributions (e.g., Dirac delta functions) which are clearly not encompassed in the functional setting of the large-scale problem considered in the previous section. The natural concept of a plastic hinge is then recovered. As noted in Section 1, the challenge is to consider these discontinuous solutions while maintaining the structure of the large-scale problem as defined by equation (2.2) in terms of the large-scale displacements $\boldsymbol{u}$. This goal can be accomplished by noting the multi-scale nature of the problem given the locality of the localized dissipative effects. The strong discontinuities become then an efficient tool for the modeling of the dissipative effects associated to the small scales of the material deformation.

In this context, we consider a local neighborhood $\mathscr{B}_{x_d} \subset \mathscr{B}$ of a material point $x_d \in \mathscr{B}$ in the large scale where the presence of a localized dissipative mechanism has been detected. Following the spectral analysis presented in Armero & Ehrlich [2002] that identifies the presence of strain softening as the triggering of the ill-posedness of the continuum model, the simulations presented in Sect. 5 consider the activation of the localized dissipative mechanism once the strain softening state is reached in a general elastoplastic hardening/softening model. We define

$$h_{x_d} = length(\mathscr{B}_{x_d}) > 0 \tag{2.7}$$

for the local neighborhood $\mathscr{B}_{x_d} \subset \mathbb{R}$. We denote by $s \in (0, h_{x_d})$ a local coordinate in $\mathscr{B}_{x_d}$ with $s = s_d$ corresponding to the original material point $x_d \in \mathscr{B}$. Figure 2.2 illustrates these ideas. The length parameter h_{x_d} is left indeterminate at this stage. The goal is to incorporate the localized dissipative effects of the "small scales" $\mathscr{B}_{x_d}$ into the large-scale problem (2.2) in the limit as $h_{x_d} \to 0$, that is, in the "large-scale limit".

To this purpose, we consider the small-scale strains ε_μ defined by

$$\boldsymbol{\varepsilon}_\mu := \boldsymbol{\varepsilon}(\boldsymbol{u}) + \boldsymbol{G}(\boldsymbol{\xi}) + \boldsymbol{\xi}\,\delta_{s_d} \qquad \text{in} \quad \mathscr{B}_{x_d}\ , \tag{2.8}$$

in terms of a set of local parameters $\xi \in \mathbb{R}^3$ and a linear operator $\boldsymbol{G}(\cdot)$ consistent with the infinitesimal assumption considered in these developments. The strains (2.8) define a local enhancement of the large-scale strains $\boldsymbol{\varepsilon}(\boldsymbol{u})$ involving, in particular, the singular measure of the Dirac delta function $\delta_{s_d}(s)$. As occurred with the length parameter h_{x_d} the strain operator $\boldsymbol{G}(\cdot)$ is left indeterminate at this stage, noting again our final goal to characterize the model in the large-scale limit $h_{x_d} \to 0$.

Given the nature of the Dirac delta function in (2.8), the local parameters $\boldsymbol{\xi}$ can be easily observed to have the units of the generalized displacements for each of the three components. In fact, they can be understood physically as the jumps of a generalized displacement distribution (say, $\boldsymbol{u}_\mu$) defined in $\mathscr{B}_{x_d}$. That is, we can consider a small-scale displacement field

$$\boldsymbol{u}_\mu = \boldsymbol{u} + \boldsymbol{\xi}\psi_{s_d} \qquad \text{in} \quad \mathscr{B}_{x_d}\ , \tag{2.9}$$

for some function $\psi_{s_d}(s)$ exhibiting a unit jump at s_d. In this way, we can write

$$\boldsymbol{\xi} = (\xi^u, \xi^w, \xi^\vartheta) = ([[u_\mu]], [[w_\mu]], [[\vartheta_\mu]])\ , \tag{2.10}$$

for the jump operator $[[\cdot]]$ at s_d. The linearity of the strain operator $\boldsymbol{G}(\cdot)$ in (2.8) follows also in the assumed infinitesimal kinematics. The consideration of compatible enhanced strains in $\mathscr{B}_{x_d}$, that is, $\boldsymbol{\varepsilon}_\mu = \boldsymbol{\varepsilon}(\boldsymbol{u}_\mu)$ appears then as a particular case.

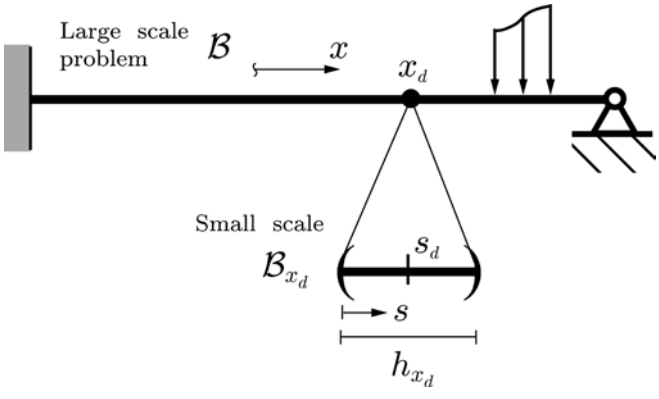

Fig. 2.2 Strong discontinuities in beams and rods. The strong discontinuities are defined locally in a neighborhood $\mathscr{B}_{x_d}$ of measure $h_{x_d} \to 0$ (the small scale) maintaining the structure of the large-scale problem

2.3 The localized dissipative mechanism

The local field $\boldsymbol{\xi}$ associated with the singular part of the strain field (2.8) allows to model directly the localized dissipative mechanism observed in the small scale $\mathscr{B}_{x_d}$ besides the large-scale response already accounted by the large-scale displacements $\boldsymbol{u}$. In this way, we consider a general inelastic model

$$\boldsymbol{\sigma}_d = \hat{\boldsymbol{\sigma}}_d(\boldsymbol{\xi}) \ , \tag{2.11}$$

between the jumps $\boldsymbol{\xi}$ and the stress resultants $\boldsymbol{\sigma}_d$ driving the localized dissipation at x_d. We recover the notion of a cohesive law as it is common in the continuum.

General plastic and damage models can be accommodated in these considerations; see Armero [1999] for a discussion in the context of continuum problems. The numerical examples presented in Sect. 5 consider a plastic model with the constitutive relation (2.11) given implicitly by the expressions

$$\left.\begin{aligned} &\dot{\boldsymbol{\xi}} = \dot{\tilde{\lambda}}\, \partial_{\boldsymbol{\sigma}_d}\tilde{\phi}, \quad \dot{\tilde{\alpha}} = \dot{\tilde{\lambda}}\, \partial_{\tilde{q}}\tilde{\phi} \\ &\tilde{\lambda} \geq 0, \quad \tilde{\phi} \leq 0, \quad \tilde{\lambda}\tilde{\phi} = 0, \quad \dot{\lambda}\dot{\tilde{\phi}} = 0 \end{aligned}\right\} \ , \tag{2.12}$$

in terms of an interaction diagram (or yield surface) $\tilde{\phi}(\boldsymbol{\sigma}_d, \tilde{q})$ function of the stress resultants $\boldsymbol{\sigma}_d$ driving the discontinuity and the localized softening internal variables $\tilde{q}$ and $\tilde{\alpha}$, related by a given localized softening law $\tilde{q} = \hat{\tilde{q}}(\tilde{\alpha})$. The Eq. $(2.12)_2$ correspond to the loading/unloading conditions and consistency conditions defining the localized plastic multiplier $\dot{\tilde{\lambda}}$.

The symbols $\dot{(\cdot)}$ are used explicitly in (2.12) to emphasize the localized nature of the field in contrast with their analogs in the continuum model (2.6). The plastic model (2.12) defines an inelastic relation between the generalized displacement jumps $\boldsymbol{\xi}$ and the driving stress resultant $\boldsymbol{\sigma}_d$. This situation is to be contrasted with the inelastic relation between the strains and stress resultants implied by the original continuum relations (2.6). In this way, we refer to the final model defined by the relation (2.11) (e.g. Eq (2.12)) as a "localized model".

Remarks 2.2.

1. Depending on the nature of the interaction diagram $\tilde{\phi}$ in (2.12) we can recover different models of plastic hinges. In this way, an interaction diagram depending only on the bending moment M_d leads to an articulation hinge where only a relative rotation ξ^{ϑ} is activated. The numerical examples in Sect. 5 consider several of these cases. In general, if the constitutive model $(2.12)_1$ defines a constant direction for the displacement jump rate (i.e. $\boldsymbol{n}_{\tilde{\phi}} := \partial_{\boldsymbol{\sigma}_d}\dot{\tilde{\phi}} = \text{constant}$), only the component of the jump along $\xi_n := \boldsymbol{\xi}\cdot\boldsymbol{n}_{\tilde{\phi}}$ evolves. In this case, the general localized relation (2.11) must be understood then for the particular component of the stress resultants and generalized displacement jump ξ_n.
2. The Eq. (2.12) model a rigid-plastic response of the strong discontinuity of the associated form. As noted above, additional effects (like elastic, viscous, damage, etc. components) can be accommodated in the framework considered here, leading eventually to what we can refer as elastoplastic, viscous, damage, etc. hinges. For simplicity, we use the generic name of "plastic hinges" in this paper. Equally important in many applications is the consideration of the plastic evolution Eq. (2.12) in combination with a multi-surface form to model corners in the interaction diagram $\tilde{\phi}(\boldsymbol{\sigma}_d, \tilde{q})$. Since these considerations do not affect the development of the finite elements discussed in Sect. 3 and 4, the main goal of this paper, further details are omitted here. We plan to present a complete discussion of these important aspects of the models considered here in a forthcoming publication. □

2.4 The local governing equation

The introduction of the new parameters $\boldsymbol{\xi}$ in $\mathscr{B}_{x_d}$ requires the consideration of a new equation in $\mathscr{B}_{x_d}$ for its determination, as developed in this section. We first note that the considerations presented in the previous section identified only the general constitutive relation (2.11) for the localized dissipative mechanism associated with the strong discontinuity at x_d. The bulk response in the local neighborhood $\mathscr{B}_{x_d}$ can be given by a general constitutive relation between the stress resultants $\boldsymbol{\sigma}$ and the local strain measures

$$\bar{\boldsymbol{\varepsilon}}_{\mu} := \boldsymbol{\varepsilon}(\boldsymbol{u}) + \boldsymbol{G}(\boldsymbol{\xi}) \ , \tag{2.13}$$

that is, the regular part of the small-scale strains (2.8) in the bulk $\breve{\mathscr{B}}_{x_d} := \mathscr{B}_{x_d}\backslash x_d$.

Without loss of generality, we consider the existence of a stress potential $W(\bar{\boldsymbol{\varepsilon}}_{\mu})$ (depending possibly on other internal variables in the bulk $\breve{\mathscr{B}}_{x_d}$) such that

$$\boldsymbol{\sigma} = \partial_{\bar{\varepsilon}_{\mu}} W \quad \text{in} \quad \mathscr{B}_{x_d} \ . \tag{2.14}$$

The numerical simulations considered in Sect. 5 consider a linear elastic response in the bulk given by

$$N = EA\bar{\varepsilon}_{\mu}, \quad M = EI\bar{\kappa}_{\mu}, \quad \text{and} \quad V = GA_s\bar{\gamma}_{\mu} \ , \tag{2.15}$$

for a linear elastic isotropic material with Young modulus E and shear modulus G, and a cross-section area A, second-moment of area I and modified area in shear A_s. The quadratic character of the stress potential $W(\bar{\boldsymbol{\varepsilon}}_{\mu})$ follows trivially in this case.

As shown in Armero [1999] and Armero [2001], the goal of introducing the dissipation associated with the localized inelastic model (2.11) in the small scale $\mathscr{B}_{x_d}$ into the large-scale problem (2.2) in the large-scale limit $h_{x_d} \to 0$ defines not only this local governing equation but also the strain operator $\boldsymbol{G}(\cdot)$ in the small-scale strain (2.8). With the above considerations at hand, we can write the relation

$$\mathscr{D}_\mu := \int_{\breve{\mathscr{B}}x_d} \left[\dot{\tilde{\boldsymbol{\varepsilon}}}_\mu \cdot \boldsymbol{\sigma} - \dot{W}\right] ds + \dot{\boldsymbol{\xi}} \cdot \boldsymbol{\sigma}_d$$
$$= \underbrace{\int_{\breve{\mathscr{B}}x_d} \left[\boldsymbol{\varepsilon}(\dot{\boldsymbol{u}}) \cdot \boldsymbol{\sigma} - \dot{W}\right] ds}_{:=\mathscr{D}} + \int_{\breve{\mathscr{B}}x_d} \boldsymbol{G}(\dot{\boldsymbol{\xi}}) \cdot \boldsymbol{\sigma}\, ds + \dot{\boldsymbol{\xi}} \cdot \boldsymbol{\sigma}_d \ . \tag{2.16}$$

The functional $\mathscr{D}_\mu$ can be identified with the dissipation functional in the small-scale whereas the functional $\mathscr{D}$ accounts only for the stress power on the large-scale strains $\varepsilon(\boldsymbol{u})$. Following the philosophy indicated in Sect. 1 (that is, our goal to solve a large-scale problem while still capturing the dissipation associated to the small scales), the identification of these two dissipations for any variations of the internal parameters $\boldsymbol{\xi}$ leads readily to the local equation

$$r_{\mathscr{B}_{x_d}}(\boldsymbol{u}, \boldsymbol{\xi}; \boldsymbol{\zeta}) := \int_{\mathscr{B}_{x_d}} \boldsymbol{G}(\boldsymbol{\zeta}) \cdot \boldsymbol{\sigma}\, ds + \boldsymbol{\zeta} \cdot \hat{\boldsymbol{\sigma}}_d(\boldsymbol{\xi}) = 0 \quad \forall \boldsymbol{\zeta} \in \mathbb{R}^3 \ , \tag{2.17}$$

in the small scale $\mathscr{B}_{x_d}$.

It remains to determine the local strain operator $\boldsymbol{G}(\cdot)$ defining the regular part of the enhanced strain (2.8). Equation (2.17) relates the stress resultant $\boldsymbol{\sigma}$ in the bulk $\mathscr{B}_{x_d}$, as seen also in the large-scale problem, with the stress resultant $\boldsymbol{\sigma}_d$ driving the localized dissipative mechanism in x_d. We note again our interest to recover the large-scale limit $h_{x_d} \to 0$ while introducing the localized dissipation in the large-scale problem through this equation in the small scale $\mathscr{B}_{x_d}$. We then impose the condition

$$\boldsymbol{\sigma}_d = \boldsymbol{\sigma}(x_d) \quad \text{as} \quad h_{x_d} \to 0 \ , \tag{2.18}$$

that is, we identify the driving stress resultants $\boldsymbol{\sigma}_d$ on the discontinuity with the stress resultants at x_d in the large-scale limit. From Eq. (2.17), we see that condition (2.18) implies the asymptotic relation

$$\boldsymbol{G}(\boldsymbol{\xi}) = -\frac{1}{h_{x_d}} \boldsymbol{\xi} + o(1) \qquad \text{as} \quad h_{x_d} \to 0 \ , \tag{2.19}$$

that is, up to higher order terms in h_{x_d} (with the common use of the "small-oh" $o(\cdot)$ notation). The model is then fully defined in the large-scale limit.

We observe that the local Eq. (2.17) defines a relation between the large-scale displacement $\boldsymbol{u}$ and the local parameters $\boldsymbol{\xi}$ through the dependence of the stress resultants $\boldsymbol{\sigma}$ on the large-scale strain measure $\varepsilon(\boldsymbol{u})$ in (2.13). The linearization of this equation leads to the relation

$$D_\xi \left(r_{\mathscr{B}_{x_d}}\right) \dot{\boldsymbol{\xi}} = \left(\frac{1}{h_{x_d}^2} \int_{\mathscr{B}_{x_d}} \mathbb{C} ds + \boldsymbol{H}\right) \dot{\boldsymbol{\xi}} + o(h_{x_d}) \quad \text{as} \quad h_{x_d} \to 0 \ , \tag{2.20}$$

where we have introduced the tangents associated to the rate relations

$$\dot{\boldsymbol{\sigma}} = \mathbb{C} \dot{\tilde{\boldsymbol{\varepsilon}}}_\mu \quad \text{and} \quad \dot{\boldsymbol{\sigma}}_d = \boldsymbol{H} \dot{\boldsymbol{\xi}} \tag{2.21}$$

for the bulk and localized responses, respectively, both at x_d. A straightforward use of the implicit function theorem implies then the existence of a relation

$$\boldsymbol{\xi} = \hat{\boldsymbol{\xi}}(\boldsymbol{u}) \ , \tag{2.22}$$

if the matrix appearing in (2.20) is not singular. The bulk response is expected to lead to a positive definite tangent stiffness $\mathbb{C}$ (e.g., positive moduli for the linear elastic response (2.15)), whereas a softening response of the localized relation (2.11) leads to the negative character of the softening moduli $\boldsymbol{H}$. Assuming a finite moduli $\boldsymbol{H}$, the matrix in (2.20) can be assured to remain positive definite by choosing a small enough h_{x_d} and, eventually, in the large-scale limit $h_{x_d} \to 0$ of interest here. We refer to Armero [2001] for additional details of these considerations in the context of a local continuum.

The introduction of the relation (2.22) in the weak Eq. (2.2) through the stress resultant relations (2.15) leads eventually to a large-scale problem in $\boldsymbol{u}$ only, involving no small scales (i.e. $h_{x_d} = 0$). We refer to the resulting problem as the "enhanced large-scale problem". Remarkably, the structure of the original large-scale problem is fully maintained while fully capturing the dissipation of the small scales of the material response. We note again that the localized models must be understood with $h_{x_d} = 0$, that is, with no small scales $\mathscr{B}_{x_d}$. The constructive procedure followed in all these arguments, involving in particular a finite $h_{x_d} > 0$, plays a crucial role in the development of the finite element methods appropriate for the numerical simulation of the final localized model, as considered in the next section. The condition (2.19) will play a crucial role then to assure the consistency of the finite elements with the proposed localized models.

Remark 2.3. The approach considered here understands the strong discontinuities as a tool for the modeling of the localized dissipative mechanisms observed in the localized failures of structures, eventually capturing these dissipative effects in the large-scale problem. In this way, the role of the displacement jump $\boldsymbol{\xi}$ in the enhanced large-scale problem follows closely the role of an internal variable in an inelastic model. However, the explicit consideration of the kinematics associated to these discontinuous solutions (as implied, e.g., by Eq. (2.8) for the small-scale strains) leads naturally to the development of efficient finite element methods for the accurate resolution of the localized failures of interest.

3 Enhanced finite element methods

The considerations presented in the previous section in the derivation of localized models are especially suited for the development of enhanced strain finite element

methods for its numerical approximation. The strong discontinuities (or plastic hinges) are incorporated in the finite element interpolations without resorting to the regularization of the Dirac delta functions appearing in the formulation, hence following similar considerations as the formulation originally presented in Armero & Garikipati [1995] for the local continuum.

We develop the general finite element framework in Sect. 3.1. Section 3.2 describes the linearization process considered in the actual numerical implementation and needed in the forthcoming sections. The actual design of the finite elements is addressed in Sect. 4.

3.1 The finite element formulation

The finite element implementation of the localized models developed in the previous section follows easily from the constructive approach considered in the formulation of these models. The identification of the local neighborhood $\mathscr{B}_{x_d}$ in the previous arguments with a finite element $\mathscr{B}_e = [x_1, x_2]$, for end nodal coordinates x_1 and x_2 resulting in an element length $h_e = x_2 - x_1$ allows this implementation. We denote by $s := x - x_1$. The element length h_e plays then the role of h_{x_d} in the arguments of the previous section. A finite length $h_e > 0$ occurs in the actual finite element simulations, but this length is to be understood as $h_e \to 0$ for a convergent analysis. The situation characteristic of the theoretical arguments of Sect. 2 is then recovered.

In this way, the analog of the small-scale strains (2.8) in the finite element context reads

$$\boldsymbol{\varepsilon}_e^h = \underbrace{\boldsymbol{B}\boldsymbol{d}_e + \boldsymbol{G}_c e}_{\bar{\boldsymbol{\varepsilon}}_e^h} + \boldsymbol{\xi}_e \delta_{s_d} \ , \tag{3.1}$$

defining an enhancement of a given base finite element defined by the linear strain operator $\boldsymbol{B}$ for a set of generalized displacements $\boldsymbol{d}_e$ in element $\mathscr{B}_e$. The enhanced part of the strains has two parts as in the small-scale strains (2.8). A singular part in terms of the Dirac delta contribution and a regular part in terms of the enhanced strain operator $\boldsymbol{G}_c$, both depending on the local enhanced parameters $\boldsymbol{\xi}_e$ in element $\mathscr{B}_{e,loc}$ where a plastic hinge has been detected. Section 4 below considers several base finite elements and discusses the design of the enhanced strain operator $\boldsymbol{G}_c$ appropriate for each of them.

The principle of virtual work governing the large-scale problem (2.2) and the local governing Eq. (2.17) in the small scales $\mathscr{B}_{e,loc}$, with $\mathscr{B}_{c,loc} := \mathscr{B}_{e,locl} \backslash x_d$ in the discrete context, lead to the nonlinear equations

$$\left.\begin{aligned} \boldsymbol{R} &:= \boldsymbol{f}^{ext} - \mathop{\mathbf{A}}_{e=1}^{n_{elem}} \int_0^{h_e} \boldsymbol{B}^T \boldsymbol{\sigma}(\boldsymbol{d}_e, \boldsymbol{\xi}_e) ds = 0, \\ \boldsymbol{r}_e &:= \int_0^{h_e} \boldsymbol{G}_e^T \boldsymbol{\sigma}(\boldsymbol{d}_e, \boldsymbol{\xi}_e) ds + \hat{\boldsymbol{\sigma}}_d(\boldsymbol{\xi}_e) = 0 \quad \text{in } \mathscr{B}_{e,loc} \ . \end{aligned}\right\} \tag{3.2}$$

The stress resultants $\boldsymbol{\sigma}(\boldsymbol{d}_e, \boldsymbol{\xi}_e)$ in the bulk are given by the generic bulk response relation (2.14) in terms of the regular part of the enhanced strains $\bar{\boldsymbol{\varepsilon}}_e^h$ in (3.1), whereas the driving stress resultants $\boldsymbol{\sigma}_d(\boldsymbol{\xi}_e)$ are given by the localized relations governing the plastic hinge. The symbol $\mathop{\mathbf{A}}_{e=1}^{n_{elem}}$ in (3.2) refers to the standard assembly operator over the n_{nelem} elements.

We observe again that the localized model developed in the previous section is defined as $h_{x_d} = h_e \to 0$. In particular, the enhanced strain operator $\boldsymbol{G}(\cdot)$ in (2.8) is only required to satisfy the asymptotic relation (2.19) as $h_{x_d} \to 0$. This situation leaves a great deal of freedom in the development of the appropriate enhanced strain interpolations for a finite $h_e > 0$. In particular, the performance of the finite element can be optimized by choosing a different enhanced strain operators in the definition of the enhanced strains (2.8) and in the local governing Eq. (2.17) imposing the local equilibrium in weak form. We refer to these operators as $\boldsymbol{G}_c(\cdot)$ and $\boldsymbol{G}_e(\cdot)$ in equations (3.1) and (3.2), respectively, as for compatibility and equilibrium operators. The requirement

$$\boldsymbol{G}_c, \boldsymbol{G}_e = -\frac{1}{h_e} 1 + \mathscr{O}(1) \quad \text{as} \quad h_e \to 0 \ , \tag{3.3}$$

appears then for the consistency with the previous arguments. We note that the consideration of these different operators may lead, a-priori, to a non-symmetric system of equations after linearization; see Sect. 3.2 below.

As a particular case, given the spatial polynomial interpolation for the stress resultants $\boldsymbol{\sigma}^h(s) := \boldsymbol{\sigma}(\boldsymbol{d}_e, \boldsymbol{\xi}_e)$ arising for the assumed interpolation in a particular finite element, we can construct the equilibrium operator $\boldsymbol{G}_e$ such that

$$\boldsymbol{\sigma}^h(s_d) = -\int_0^{h_e} \boldsymbol{G}_e^T \boldsymbol{\sigma}^h(s) ds \ .$$

In this way, the Eq. $(2.17)_2$ imposes exactly the pointwise relation $\boldsymbol{\sigma}_d = \boldsymbol{\sigma}^h(s_d)$ for the driving stress resultant at the discontinuity. For example, for a stress resultant $\boldsymbol{\sigma}^h(s)$ involving linear functions in s at the most, we have

$$\begin{aligned} &\boldsymbol{G}_e = -\frac{g_e(s)}{h_e} 1 \\ &\text{for} \quad g_e(s) = 1 + 3\left(1 - \frac{2s_d}{h_e}\right)\left(1 - \frac{2s}{h_e}\right) \ , \end{aligned} \tag{3.4}$$

after noting that

$$\begin{aligned} &\frac{1}{h_e}\int_0^{h_e} g_e(s) ds = 1 \qquad \text{and} \\ &\frac{1}{h_e}\int_0^{h_e} s g_e(s) ds = s_d \ . \end{aligned} \tag{3.5}$$

A similar function can be found for polynomials of any degree; see Appendix I for additional details. We

observe that the (equilibrium) enhanced strain operator (3.4) does satisfy the consistency requirement (3.3).

Remarks 3.1

1. The above numerical implementation is simplified for the particular case of a constant direction of the evolution of the displacement jumps described in Remark 2.2.1. In this case, the single component ξ_n of the enhanced parameters is considered, with Eq. $(3.2)_2$ projected in the direction $\boldsymbol{n}_{\tilde{\phi}} := \partial_{\boldsymbol{\sigma}_d}\tilde{\phi}$ as well. These considerations affect the definitions of the enhanced strain operators $\boldsymbol{G}_c$ and $\boldsymbol{G}_e$.
2. The spectral analysis presented in Armero & Ehrlich [2002] identifies the presence of strain softening as the triggering of the ill-posedness of the continuum inelastic problem. For the case of an elastic-softening response considered in the numerical examples of Sect. 5, the strong discontinuity (plastic hinge) is then activated where yielding is observed.
3. Different finite elements are developed in Sect. 4. The (reduced integration) constant strain element of Sect. 4.3 considers a one-point integration quadrature rule with the quadrature point at the center of the element ($s = h_e/2$). For the rest of elements, involving a linear strain distribution at the most, we use the three-point Lobatto quadrature (see e.g., Hughes [1987], page 440), with one quadrature point at each end node and a third one at the center of the element. The plastic hinge is activated in the quadrature point where it is detected; see Item 2. above. In this way, for an element with a linear distribution of the yield function $\tilde{\phi}(\boldsymbol{\sigma}_d, 0)$ (e.g., linear interpolation of the bending moment for an interaction diagram based on the bending moment only), the hinge is first activated at either end. When this detection is simultaneous at several quadrature points due to a constant interpolation of the yield function $\tilde{\phi}(\boldsymbol{\sigma}_d, 0)$, the discontinuity is activated at the middle quadrature point. □

3.2 The discrete linearized equations

The nonlinear set of algebraic Eq. (3.2) are solved through a Newton-Raphson iterative scheme. To this purpose, we consider their consistent linearization

$$\underbrace{\begin{bmatrix} \boldsymbol{K}_{dd} & \boldsymbol{K}_{d\xi} \\ \boldsymbol{K}_{\xi d} & \boldsymbol{K}_{\xi\xi} \end{bmatrix}}_{\boldsymbol{K}} \begin{bmatrix} \Delta\boldsymbol{d}^{(i)}_{n+1} \\ \Delta\boldsymbol{\xi}^{(i)}_{n+1} \end{bmatrix} = \begin{bmatrix} \boldsymbol{R}^{(i)}_{n+1} \\ -\boldsymbol{r}^{(i)}_{n+1} \end{bmatrix} , \tag{3.6}$$

in the increments of the nodal displacements and enhanced parameters

$$\boldsymbol{d}^{(i+1)}_{n+1} = \boldsymbol{d}^{(i)}_{n+1} + \Delta\boldsymbol{d}^{(i)}_{n+1} \quad \text{and} \quad \boldsymbol{\xi}^{(i+1)}_{n+1} = \boldsymbol{\xi}^{(i)}_{n+1} + \Delta\boldsymbol{\xi}^{(i)}_{n+1} , \tag{3.7}$$

respectively, in an increment n (say, $[t_n, t_{n+1}]$) and iteration counter (i). The stiffness matrices in (3.6) are defined by the element contributions

$$\left.\begin{aligned} \boldsymbol{K}_{e,dd} &= \int_0^{h_e} \boldsymbol{B}^T \mathbb{C} \boldsymbol{B} ds, & \boldsymbol{K}_{e,d\xi} &= \int_0^{h_e} \boldsymbol{B}^T \mathbb{C} \boldsymbol{G}_c ds, \\ \boldsymbol{K}_{e,\xi d} &= \int_0^{h_e} \boldsymbol{G}_e^T \mathbb{C} \boldsymbol{B} ds, & \boldsymbol{K}_{e,\xi\xi} &= \int_0^{h_e} \boldsymbol{G}_e^T \mathbb{C} \boldsymbol{G}_c ds + \boldsymbol{H} , \end{aligned}\right\} \tag{3.8}$$

for the tangent tensors $\mathbb{C}$ and $\boldsymbol{H}$ defined in (2.21) for the rate form of the bulk and localized responses, respectively, at the known solution $\{\boldsymbol{d}^{(i)}_{n+1}, \boldsymbol{\xi}^{(i)}_{n+1}\}$. We have omitted the increment and iteration indices when referring to the different stiffness matrices to simplify the notation.

We observe that the enhanced parameters only affect the elements where a plastic hinge has been detected. In fact, the local character of the enhanced Eq. $(3.2)_2$ for each of such elements allows to solve the corresponding linearized Eq. $(3.6)_2$ for $\Delta\boldsymbol{\xi}^{(i)}_{e,n+1}$ locally in each element $\mathscr{B}_{e,loc}$, leading to the relation

$$\Delta\boldsymbol{\xi}^{(i)}_{e,n+1} = -\boldsymbol{K}^{-1}_{e,\xi\xi}\left[\boldsymbol{r}^{(i)}_{e,n+1} + \boldsymbol{K}_{e,\xi d}\Delta\mathbf{d}^{(i+1)}_{e,n+1}\right] \quad \text{in } \mathscr{B}_{e,loc} . \tag{3.9}$$

This situation allows the static condensation of these parameters after introducing (3.9) in $(3.6)_1$ resulting in the reduced system

$$\boldsymbol{K}^*\Delta\mathbf{d} = \boldsymbol{R}^{*(i)}_{n+1} , \tag{3.10}$$

for the statically condensed stiffness matrix

$$\boldsymbol{K}^* = \mathop{A}_{e=1}^{n_{\text{elem}}}\left[\boldsymbol{K}_{e,\text{dd}} - \boldsymbol{K}_{e,\text{d}\xi}\boldsymbol{K}^{-1}_{e,\xi\xi}\boldsymbol{K}_{e,\xi\text{d}}\right] , \tag{3.11}$$

and the statically condensed residual

$$\boldsymbol{R}^{*(i)}_{n+1} = \mathop{A}_{e=1}^{n_{\text{elem}}}\left[\boldsymbol{R}^{(i)}_{e,n+1} + \boldsymbol{K}^{-1}_{e,\xi\xi}\boldsymbol{r}^{(i)}_{e,n+1}\right] , \tag{3.12}$$

obtained both through the assembly of the n_{elem} elements. We note that the consideration of different enhanced strain operators $\boldsymbol{G}_e \neq \boldsymbol{G}_c$ leads, in general, to a non-symmetric system of Eq. (3.10), except in special situations where the integrations in (3.8) eventually results in this symmetry, as it is the case for the element proposed in Sect. 4.4.

The arguments considered in the development of the localized models in Sect. 2 to arrive at a "enhanced large-scale problem" translate then directly in the actual finite element implementation. Eq. (3.10) defines a problem in terms of the nodal (or, better, large-scale) displacements $\boldsymbol{d}$. The computational efficiency of the proposed approach is to be noted.

4 Design of locking-free enhanced finite elements

It remains to determine the operator $\boldsymbol{G}_c$ defining the enhanced strains (3.1) locally in a finite element. A simple choice, given the consistency condition (3.3), is given by

$$\boldsymbol{G}_c^{(E)} := -\frac{1}{h_e}\mathbf{1} \ . \tag{4.1}$$

We refer to the final strategy as the "E" enhancement and label the resulting enhanced finite elements by "-E". The enhancement (4.1) can be thought as a direct extension of similar considerations from previously proposed formulations for the continuum involving the leading h_e^{-1} term (see e.g., Armero & Garikipati [1995, 96]), Armero [1999]. However, the coupled (or linked) character of the transverse shear and bending strains noted in Sect. 2.1 leads to non-optimal finite elements for finite h_e, even though a consistent formulation is obtained for $h_e \to 0$. The "E" enhancement (4.1) may lead, in particular, to stress locking as elaborated in Sect. 4.1 below.

We develop in this section several enhanced finite elements avoiding these difficulties. To illustrate the relation of the different enhancements with the basic interpolations of the underlying finite elements, we present first the case of a simple two-noded interpolation of the generalized displacements in Sect. 4.2. This finite element exhibits the well-known shear locking in the thin-beam limit, even in the context of the elastic problem. The reduced one-point integration, constant strain element is then investigated in Sect. 4.3 to avoid this drawback. Furthermore, we consider in Sect. (4.4) the more sophisticated finite element involving a linked interpolation of the deflection and rotation fields as presented in Crisfield [1984].

4.1 Stress locking

The kinematics of the finite element should allow, for finite $h_e > 0$, the resolution of the zero state of strain (in its regular part) corresponding to a fully softened state of the plastic hinge (i.e. $\boldsymbol{\sigma}_d = 0$). Otherwise, a spurious transfer of stresses occurs which is known as stress locking. An over-stiff response of the element is then observed in this case, even though its effects may be diminished as the finite element mesh is refined (i.e. as $h_e \to 0$).

This basic consideration defines the design strategy for the enhanced finite elements presented in this work. Figure 4.1 depicts a typical two-noded finite element with a plastic hinge at the local coordinate s_d. The plastic hinge exhibits a generalized displacement jump $\hat{\boldsymbol{\xi}}_e = (\hat{\xi}_e^u, \hat{\xi}_e^w, \hat{\xi}_e^\vartheta)$. For an axial displacement $\hat{u}_1$, rotation $\hat{\vartheta}_1$ and deflection $\hat{w}_1$ for the first node, the displacements for the second node associated to zero strains are given by

$$\left.\begin{aligned} \hat{u}_2 &= \hat{u}_1 + \hat{\xi}_e^u, \\ \hat{\vartheta}_2 &= \hat{\vartheta}_1 + \hat{\xi}_e^\vartheta, \\ \hat{w}_2 &= \hat{w}_1 + \hat{\vartheta}_1 h_e + \hat{\xi}_e^w + (h_e - s_d)\hat{\xi}_e^\vartheta \ , \end{aligned}\right\} \tag{4.2}$$

with a piece-wise constant distribution of the axial and rotation fields on both sides of the element and a piece-wise linear distribution of the transversal displacement. That is, we have the small-scale displacements (i.e. at the element level)

$$\left.\begin{aligned} \hat{u}_\mu(s) &= \hat{u}_1 + H_{s_d}(s)\,(\hat{u}_2 - \hat{u}_1), \\ \hat{\vartheta}_\mu(s) &= \hat{\vartheta}_1 + H_{s_d}(s)\,(\hat{\vartheta}_2 - \hat{\vartheta}_1), \\ \hat{w}_\mu(s) &= \hat{w}_1 + \hat{\vartheta}_1\, s + H_{s_d}(s) \\ &\quad \times \left[(\hat{w}_2 - \hat{w}_1) - \hat{\vartheta}_1\, s - \hat{\vartheta}_2\,(h_e - s)\right] \ , \end{aligned}\right\} \tag{4.3}$$

in terms of the displacements of the end nodes $\hat{\boldsymbol{u}}_1$ and $\hat{\boldsymbol{u}}_2$ given by (4.2), and the Heaviside jump function

$$\boldsymbol{H}_{s_d}(S) := \begin{cases} 0 & \text{for } s < s_d \ , \\ 1 & \text{for } s > s_d \ . \end{cases} \tag{4.4}$$

A straightforward calculation based on the definition of the strain measures (2.1) shows their vanishing for the displacement distributions (4.3). Equivalently, we can define the jump components

$$\left.\begin{aligned} \hat{\xi}_e^u &= \hat{u}_2 - \hat{u}_1, \\ \hat{\xi}_e^\vartheta &= \hat{\vartheta}_2 - \hat{\vartheta}_1, \\ \hat{\xi}_e^w &= \hat{w}_2 - \hat{w}_1 - \hat{\vartheta}_1 s_d - \hat{\vartheta}_2(h_e - s_d) \ , \end{aligned}\right\} \tag{4.5}$$

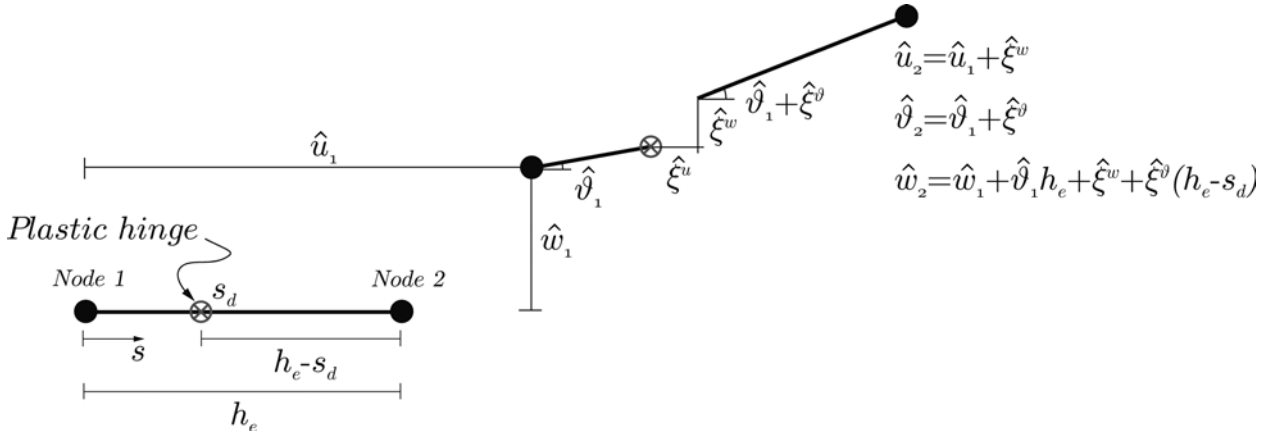

Fig. 4.1 Sketch of the plastic hinge mode. A fully softened plastic hinge $\boldsymbol{\sigma}_d = 0$ should be captured for a zero strain (stress resultant) in the bulk of the element, that is, for the end nodal displacements shown in terms of the displacement jumps $\hat{\boldsymbol{\xi}} = (\hat{\xi}^u, \hat{\xi}^w, \hat{\xi}^\vartheta)$ at the plastic hinge

associated to the nodal displacements (4.2). We refer to the distributions $\hat{\boldsymbol{u}}_\mu(s)$ in (4.3) and, in particular, to the nodal displacements (4.2) as the "hinge mode".

Starting with a base finite element able to reproduce linear displacements, its enhanced counterpart must be able to reproduce exactly this hinge mode with zero strain in its regular part (i.e., besides the singular strain associated with the discontinuity or hinge). Crucial to this property is the proper definition of the enhanced strain operator $\boldsymbol{G}_c$ defining in combination with the (compatible) strain operator $\boldsymbol{B}$ the element strains (3.1). The imposition of zero regular part of the strain for the displacement distributions (4.3) defines then the proper enhanced strain operator $\boldsymbol{G}_c$. Different base elements, that is, different $\boldsymbol{B}$'s will lead then to different enhanced strain operators $\boldsymbol{G}_c$'s.

The sections below show how these arguments define efficient locking-free finite elements for the modeling of plastic hinges in beams and frames. The proposed general principle is illustrated for particular finite elements. We point out again the basic consistency requirement (3.3) that the newly proposed enhanced strain operators $\boldsymbol{G}_c$ must satisfy as $h_e \to 0$. The leading term in h_e must be then given by (4.1).

Clearly, the enhancement for the uncoupled axial component defined by (4.1) is enough to avoid the stress-locking in the axial alone: the value $\xi^u = \hat{u}_2 - \hat{u}_1$ reproduces trivially the zero axial strain associated with the piece-wise constant axial displacement distribution of the hinge mode (4.3). Similar considerations apply to the bending strain and the rotation enhancement. This situation is not so trivial for the transverse shear strain. The linking between the jumps in the rotation and the deflection in (4.2) is to be noted, requiring then more involved enhanced strain operators when compared with the basic "E" enhancement (4.1). A linking between the rotation and deflection jumps is then to be expected, as illustrated in the examples of the sections below. Given this linked nature of the final enhanced strain operator $\boldsymbol{G}_c$, we refer to the new enhancement strategies as "LE" enhancement ("linked enhancement") in contrast with the "E" enhancement (4.1).

4.2 Constant axial, constant bending, linear transverse shear finite elements (N0M0S1)

The simplest finite element for a Timoshenko beam/rod consists of the two-noded piece-wise linear interpolation of the generalized displacements

$$\left.\begin{aligned} u^h(s) &= \left(1-\frac{s}{h_e}\right)u_1 + \frac{s}{h_e}u_2, \\ \vartheta^h(s) &= \left(1-\frac{s}{h_e}\right)\vartheta_1 + \frac{s}{h_e}\vartheta_2, \\ w^h(s) &= \left(1-\frac{s}{h_e}\right)w_1 + \frac{s}{h_e}w_2 \ , \end{aligned}\right\} \tag{4.6}$$

for a typical element $\mathscr{B}_e = [x_1, x_2]$ (with $s := x - x_1$ and $h_e := x_2 - x_1$, as before), the nodal axial displacements u_1 and u_2, the nodal deflections w_1 and w_2, and the nodal rotations ϑ_1 and ϑ_2. The displacements (4.6) are to be understood as a numerical approximation of the large-scale displacements $\boldsymbol{u}$ in Sect. 2.1 .

The regular part of the enhanced strains (2.8) in the elements where the strong discontinuity has been detected is then given by

$$\left.\begin{aligned} \bar{\varepsilon}^h_\mu(s) &= \frac{1}{h_e}(u_2 - u_1) + G^\varepsilon_c(\boldsymbol{\xi}_e), \\ \bar{\kappa}^h_\mu(s) &= \frac{1}{h_e}(\vartheta_2 - \vartheta_1) + G^\kappa_c(\boldsymbol{\xi}_e), \\ \bar{\gamma}^h_\mu(s) &= \frac{1}{h_e}(w_2 - w_1) - \left(1-\frac{s}{h_e}\right)\vartheta_1 \\ &\quad - \frac{s}{h_e}\vartheta_2 + G^\gamma_c(\boldsymbol{\xi}_e) \ , \end{aligned}\right\} \tag{4.7}$$

for the different components of the enhanced strain operator $\boldsymbol{G}_c(\boldsymbol{\xi}_e) = \left(G^\varepsilon_c(\boldsymbol{\xi}_e),\ G^\kappa_c(\boldsymbol{\xi}_e),\ G^\gamma_c(\boldsymbol{\xi}_e)\right)$. We note that the compatible (or large-scale) part of the axial and bending strains is constant, with the corresponding transverse shear part being linear in s, thus the name N0M0S1 given to the element.

Inserting then the nodal displacements (4.2) in the expressions (4.7) and requiring these strain measures to vanish, we obtain

$$\left.\begin{aligned} G^{(LE)^\varepsilon}_{c,\mathrm{N0M1S0}}(\boldsymbol{\xi}_e) &= -\frac{1}{h_e}\xi^u_e, \\ G^{(LE)^\kappa}_{c,\mathrm{N0M1S0}}(\boldsymbol{\xi}_e) &= -\frac{1}{h_e}\xi^\vartheta_e, \\ G^{(LE)^\gamma}_{c,\mathrm{N0M1S0}}(\boldsymbol{\xi}_e) &= -\frac{1}{h_e}\xi^w_e - \left(1-\frac{s+s_d}{h_e}\right)\xi^\vartheta_e \ , \end{aligned}\right\} \tag{4.8}$$

for the enhanced strain operator $\boldsymbol{G}^{(LE)}_{c,\mathrm{N0M1S0}}(\xi_e)$. The expected linking between the deflection and rotation jumps appears in the enhancement of the transverse shear strain, motivating again the name of "LE" enhancement. We refer to the final element as the N0M1S0-LE element, in contrast with the N0M1S0-E element constructed with the large-scale displacements (4.7) in combination with the enhancement (4.1). We observe that the "LE" enhancement operator (4.8) satisfies the consistency requirement (3.3) as $h_e \to 0$, reducing to the "E" enhancement (4.1) in this limit.

The strains (4.7) can be integrated, leading to the generalized displacements at the element level

$$\left.\begin{aligned} u^h_\mu(s) &= u^h(s) + \left(H_{s_d}(S) - \frac{s}{h_e}\right)\xi^u_e, \\ \vartheta^h_\mu(s) &= \vartheta^h(s) + \left(H_{s_d}(S) - \frac{s}{h_e}\right)\xi^\vartheta_e, \\ w^h_\mu(s) &= w^h(s) + \left(H_{s_d}(S) - \frac{s}{h_e}\right)\xi^w_e \\ &\quad + \left[(s-s_d)H_{s_d}(S) - \left(1-\frac{s_d}{h_e}\right)s\right]\xi^\vartheta_e \ , \end{aligned}\right\} \tag{4.9}$$

for the Heaviside function H_{s_d} defined in (4.4). Here we have imposed the nodal values $\boldsymbol{u}^h_\mu(0) = \boldsymbol{u}_1$ and $\boldsymbol{u}^h_\mu(h_e) = \boldsymbol{u}_2$. The generalized displacements (4.9) correspond to the small-scale displacements (2.9), identifying in the process the function $\psi_{s_d}(s)$ in this equation for the element under consideration and finite $h_e > 0$. The regular part of the strain measures associated with the generalized displacements (4.9) are given by the enhanced strains (4.8), with the singular parts corresponding to the Dirac delta contributions in (2.8); note that $\frac{\mathrm{d}}{\mathrm{d}s} H_{s_d} = \delta_{s_d}(s)$. We observe that introducing the jump components (4.5) in (4.9) we recover exactly the generalized displacements distributions (4.3) of the hinge mode.

4.2.1 Eigenvalue analysis

Further insight on the properties of the finite elements can be obtained through an eigenvalue analysis of the stiffness matrices arising upon linearization, as obtained in Sect. 3.2. We are interested here in the consideration of a fully softened plastic hinge. The case of vanishing stiffness in the rate response of the hinge $(2.21)_2$, leading to $\boldsymbol{H} = 0$ in (3.8), is then considered in what follows.

The calculation of the eigenvalues of the original uncondensed stiffness matrix $\boldsymbol{K}$ in (3.6) for the N0M0S1-LE element leads to six zero eigenvalues with the eigenvectors spanning the kernel of the stiffness matrix. This kernel is given by

$$
\begin{aligned}
&\mathrm{kern}[\boldsymbol{K}^{(LE)}_{\mathrm{N0M1S0}}] \\
&= \mathrm{span}\begin{bmatrix}
1 & 0 & 0 & 0 & 0 & 0 \\
0 & 1 & 0 & 0 & 0 & 0 \\
0 & 0 & 1 & 0 & 0 & 0 \\
1 & 0 & 0 & 1 & 0 & h_e - s_d \\
0 & 1 & h_e & 0 & 1 & 1 \\
0 & 0 & 1 & 0 & 0 & 0 \\
0 & 0 & 0 & 1 & 0 & 0 \\
0 & 0 & 0 & 0 & 1 & 0 \\
0 & 0 & 0 & 0 & 0 & 1
\end{bmatrix}
\begin{matrix}
(\leftarrow \Delta u_1) \\
(\leftarrow \Delta w_1) \\
(\leftarrow \Delta \vartheta_1) \\
(\leftarrow \Delta u_2) \\
(\leftarrow \Delta w_2) \\
(\leftarrow \Delta \vartheta_2) \\
(\leftarrow \Delta \xi^u_e) \\
(\leftarrow \Delta \xi^w_e) \\
(\leftarrow \Delta \xi^\vartheta_e)
\end{matrix}
\end{aligned}
\tag{4.10}
$$

for the N0M0S1-LE element. The first three columns correspond to the original rigid body modes of the base element with no additional opening of the plastic hinge: the first two columns correspond to the longitudinal and transversal translations of the element, respectively, whereas the third column corresponds to a rigid rotation around the first node. Three new zero-energy modes appear in the formulation, as it is expected from physical grounds for a fully softened hinge if the element is not to show stress locking. The fourth column corresponds to the pure opening of the discontinuity in the longitudinal direction, the fifth column to the pure opening in the transversal direction, and the last column to the articulation of the element about the hinge at s_d. Figure 4.2 depicts these six zero-energy modes.

For the N0M0S1-E, with no linked enhancement in the transverse shear strain, the element only possesses five zero-energy modes, even for the fully softened hinge. The articulation zero-energy mode, the last column in (4.10), is no longer present in the kernel of the stiffness matrix of the element. The absence of this extra zero-energy mode results in the element exhibiting stress locking. The corresponding non-zero eigenvalue is given by

$$
\begin{aligned}
&112 h_e \Big[GAs h_e^2 + 18EI \\
&\quad + \sqrt{(GAs)^2 h_e^4 + 12(GAs)(EI) h_e^2 + 324(EI)^2} \Big] \underset{h_e \to 0}{\longrightarrow} 0 \ ,
\end{aligned}
\tag{4.11}
$$

that is, vanishing for $h_e = 0$. This result shows the nature of the stress locking, gradually disappearing as the mesh is refined.

4.3 Constant axial, constant bending, constant transverse shear finite element (N0M0S0)

The N0M0S1 elements considered in the previous section, with their simple piece-wise linear interpolation of the transverse shear force in combination with the piece-wise constant bending moment distribution, show the classical shear locking in the thin-beam limit, that is, for $(GA_s h_e^2/EI) \to \infty$ in the context of the linear elastic model defined by the relations (2.15). A simple strategy

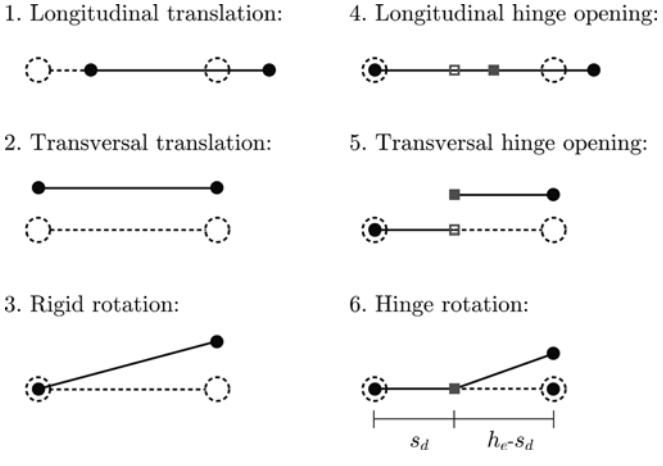

Fig. 4.2 The six zero energy modes associated to a fully softened hinge at s_d for the N0M1S0-LE element. These modes are given by the columns in (4.10), with the numbering following the order of the columns in this equation. The first three modes correspond to the rigid body modes whereas the last three correspond to the pure opening of the hinge in the longitudinal and transversal directions, and the pure hinge rotation

to avoid this shear locking is the consideration of the linear interpolations (4.6) but in combination with a one-point integration rule (with the quadrature point at the center of the element $s = h_e/2$) to evaluate the different integrals of the finite element equations. In this way, we arrive at a constant transverse shear distribution as well.

Following the logic described in Remark 3.1.3, the plastic hinges are activated at the center of the element $s_d = h_e/2$ given the constant character of the strain measures (and hence the stress resultants). In this case, the "LE" enhanced operator (4.8), evaluated also at the center of the element, reduces to the "E" enhancement (4.1), that is, we have

$$\boldsymbol{G}_{c,\mathrm{N0M0S0}}^{(LE)} = \boldsymbol{G}_c^{(E)} \ . \tag{4.12}$$

The final constant enhanced strains read in this case

$$\left.\begin{aligned} \bar{\varepsilon}_\mu^h(s) &= \frac{1}{h_e}(u_2 - u_1) - \frac{1}{h_e}\xi_e^u, \\ \bar{\kappa}_\mu^h(s) &= \frac{1}{h_e}(\vartheta_2 - \vartheta_1) - \frac{1}{h_e}\xi_e^\vartheta, \\ \bar{\gamma}_\mu^h(s) &= \frac{1}{h_e}(w_2 - w_1) - \frac{\vartheta_1 + \vartheta_2}{2} - \frac{1}{h_e}\xi_e^w \ , \end{aligned}\right\} \tag{4.13}$$

in terms of the nodal values of the generalized displacements and their jumps.

We note that the equilibrium operator $\boldsymbol{G}_e$ in (3.4) is also given in this case by $\boldsymbol{G}_e = -(1/h_e)\mathbf{1}$ recovering the symmetry of linearized system of Eq. (3.11). We refer to the resulting finite element N0M0S0-E ($\equiv$ N0M0S0-LE), and we do not expect any problems with stress locking given the arguments above.

Remark 4.1. An eigenvalue analysis for the NOM0S0-E element as presented in Sect. 4.2.1 for the N0M0S1 elements reveals the presence again of three additional zero-energy modes for the fully softened hinge, thus confirming the lack of stress locking in the element. In fact, the same exact eigenvectors as in (4.10) are recovered in this case with $s_d = h_e/2$ corresponding to the location of the hinge at the center of the element.

4.4 Constant axial, linear bending, constant transverse shear finite elements (N0M1S0)

Despite the locking-free response of the N0M0S0 element of the previous section, the simple constant strain approximation leads to a relatively poor performance. Alternatives improving on this numerical performance include the element presented in Crisfield [1984] based on a linked interpolation of the deflection and rotation fields, and a constant transverse shear strain distribution combined with a linear distribution of the bending strain. The interpolations for the generalized displacements are given by

$$\left.\begin{aligned} u^h(s) &= \left(1 - \frac{s}{h_e}\right)u_1 + \frac{s}{h_e}u_2, \\ \vartheta^h(s) &= \left(1 - \frac{s}{h_e}\right)\vartheta_1 + \frac{s}{h_e}\vartheta_2 + 4\frac{s}{h_e}\left(1 - \frac{s}{h_e}\right)\vartheta_{12}, \\ w^h(s) &= \left(1 - \frac{s}{h_e}\right)w_1 + \frac{s}{h_e}w_2 - \frac{s}{2}\left(1 - \frac{s}{h_e}\right)(\vartheta_2 - \vartheta_1) \\ &\quad + \frac{2}{3}s\left(\frac{2}{h_e}s - 1\right)\left(1 - \frac{s}{h_e}\right)\vartheta_{12} \ , \end{aligned}\right\} \tag{4.14}$$

for a typical finite element of length h_e. The element degrees of freedom correspond then to the generalized displacements at the nodes plus a bubble term in the rotation given by ϑ_{12}, which is eventually statically condensed out.

The particular interpolation considered in (4.14) results in a locking-free element in shear with a linear distribution of the bending strain and a constant distribution of the axial and transverse shear strains. With the addition of the enhanced strain terms, we obtain

$$\left.\begin{aligned} \bar{\varepsilon}_\mu^h(s) &= \frac{1}{h_e}(u_2 - u_1) + G_c^\varepsilon(\boldsymbol{\xi}_e), \\ \bar{\kappa}_\mu^h(s) &= \frac{1}{h_e}(\vartheta_2 - \vartheta_1) - \frac{8}{h_e^2}\left(s - \frac{h_e}{2}\right)\vartheta_{12} + G_c^\kappa(\boldsymbol{\xi}_e), \\ \bar{\gamma}_\mu^h(s) &= \frac{1}{h_e}(w_2 - w_1) - \frac{1}{2}(\vartheta_1 + \vartheta_2) - \frac{2}{3}\vartheta_{12} + G_c^\gamma(\boldsymbol{\xi}_e) \ , \end{aligned}\right\} \tag{4.15}$$

for the regular part of the enhanced strains (3.1). The imposition again of the requirement that the strains (4.15) vanish for the generalized displacements (4.2), with $\hat{\vartheta}_{12} = 0$, defines the enhanced strain operators

$$\left.\begin{aligned} G_{c,\mathrm{N0M0S1}}^{(LE)^\varepsilon}(\boldsymbol{\xi}_e) &= -\frac{1}{h_e}\xi_e^u, \\ G_{c,\mathrm{N0M0S1}}^{(LE)^\kappa}(\boldsymbol{\xi}_e) &= -\frac{1}{h_e}\xi_e^\vartheta, \\ G_{c,\mathrm{N0M0S1}}^{(LE)^\gamma}(\boldsymbol{\xi}_e) &= -\frac{1}{h_e}\xi_e^w - \left(\frac{1}{2} - \frac{s_d}{h_e}\right)\xi_e^\vartheta \ . \end{aligned}\right\} \tag{4.16}$$

We observe that these enhancements satisfy the consistency requirement $\boldsymbol{G}_c = -(1/h_e)\mathbf{1} + o(1)$ as $h_e \to 0$. The difference with the enhanced strains (4.8) for the linear element is to be noted. We denote the resulting enhanced strain finite element by N0M1S0-LE, in contrast with the N0M1S0-E based on the enhancement (4.1), that is, the first terms in (4.16).

The enhanced strains (4.16) can be alternatively obtained by considering the local generalized displacements

$$\left.\begin{aligned} u^h_\mu(s) &= u^h(s) + \left(H_{s_d}(S) - \frac{s}{h_e}\right)\xi^u_e, \\ \vartheta^h_\mu(s) &= \vartheta^h(s) + \left(H_{s_d}(S) - \frac{s}{h_e}\right)\xi^\vartheta_e, \\ w^h_\mu(s) &= w^h(s) + \left(H_{s_d}(S) - \frac{s}{h_e}\right)\xi^w_e \\ &\quad + \left[(s-s_d)H_{s_d}(S) - \left(\frac{1}{2} + \frac{s}{2h_e} - \frac{s_d}{h_e}\right)s\right]\xi^\vartheta_e \ . \end{aligned}\right\} \tag{4.17}$$

We note again the difference of these distributions with the small-scale displacements (4.9) for the original N0M0S1 element.

Remark 4.2.

1. Remarkably, the same element is obtained with the choice $\boldsymbol{G}_e \leftarrow \boldsymbol{G}^{(LE)}_{c,\mathrm{N0M1S0}}$ for the enhanced strain operator imposing the equilibrium in the local equilibrium equation (3.2), under the assumptions of no external distributed moments and constant material properties along the element. In this case, the linear bending moment distribution $M(s)$ arising from the linear bending strain $(4.15)_2$ and the constant transverse shear strain V arising from the constant transverse shear strain $(4.15)_3$ are related by

$$M(s) = \bar{M} - \left(s - \frac{h_e}{2}\right)V \qquad \text{for}$$

$$\bar{M} := \frac{1}{h_e}\int_0^{h_e} M(s)\mathrm{d}s = M(\frac{h_e}{2}) \ , \tag{4.18}$$

that is, $V = -\mathrm{d}M/\mathrm{d}s$. The relation (4.18) follows easily from the weak equilibrium equation associated to the variation of the bubble in the rotation $\delta\vartheta_{12}$, which reads (for no external distributed bending moments)

$$\int_0^{h_e}\left[-\frac{8}{h_e^2}\left(s - \frac{h_e}{2}\right)M(s) - \frac{2}{3}V\right]\mathrm{d}s = 0 \ , \tag{4.19}$$

after noting the dependence of the strain measures (4.15) on ϑ_{12}. Then, we obtain

$$\begin{aligned} &\int_0^{h_e}\left(\boldsymbol{G}^{(LE)}_{c,\mathrm{N0M1S0}}(\delta\xi^\vartheta_e)\right)^T\sigma\mathrm{d}s \\ &\quad= \int_0^{h_e}\left[-\frac{1}{h_e}M(s) - \left(\frac{1}{2} - \frac{s_d}{h_e}\right)V\right]\delta\xi^\vartheta_e\mathrm{d}s \\ &\quad= -\left[\underbrace{\bar{M} - \left(s_d - \frac{h_e}{2}\right)V}_{M(s_d)}\right]\delta\xi^\vartheta_e \\ &\quad= \int_0^{h_e}\left(\boldsymbol{G}_e(\delta\xi^\vartheta_e)\right)^T\sigma\mathrm{d}s \ . \end{aligned} \tag{4.20}$$

A similar result for the other two components of equation $(3.2)_2$ (i.e. for $\delta\xi^u_e$ and $\delta\xi^w_e$) follows easily. Hence, the driving stress resultant on the plastic hinge is given by the stress resultant at that point with the choice $\boldsymbol{G}_e \leftarrow \mathbf{G}^{(LE)}_{c,\mathrm{N0M1S0}}$. A major consequence of this result is that the N0M1S0-LE element leads to a symmetric system of equations (3.11), regardless of the position of the discontinuity.

2. We observe that the N0M1S0-E element can accommodate zero strain measures (4.15) with $\hat{\vartheta}_{12} = 0$ and the jumps

$$\left.\begin{aligned} \hat{\xi}^u_{e,\mathrm{approx}} &= \hat{u}_2 - \hat{u}_1 = \hat{\xi}^u_e, \\ \hat{\xi}^\vartheta_{e,\mathrm{approx}} &= \hat{\vartheta}_2 - \hat{\vartheta}_1 = \hat{\xi}^\vartheta_e, \\ \hat{\xi}^w_{e,\mathrm{approx}} &= \hat{w}_2 - \hat{w}_1 - \frac{h_e}{2}(\hat{\vartheta}_1 + \hat{\vartheta}_2) \\ &= \hat{\xi}^w_e + \left(\frac{h_e}{2} - s_d\right)(\hat{\vartheta}_2 - \hat{\vartheta}_1) \ , \end{aligned}\right\} \tag{4.21}$$

for the original jumps $\hat{\boldsymbol{\xi}}_e$ in (4.5) of the hinge mode. This is a direct consequence of the constant transverse shear in the base element. Hence, the N0M1S0-E element is able to reproduce a hinge mode with no strain, but not in terms of the exact jump components. We note the difference of the jumps $\hat{\boldsymbol{\xi}}_{e,\mathrm{approx}}$ in (4.21) with the exact jumps in (4.5) when the discontinuity is not at the center of the element $s_d \neq h_e/2$ while exhibiting a jump in the rotation field. This situation implies that the N0M1S0-E will not show stress-locking, but it will not capture the exact solution for a finite mesh $h_e > 0$ and a hinge involving a rotation jump component unless the plastic hinge forms at the center of the element. The exact solution is recovered in the limit $h_e \to 0$. These considerations are confirmed by the numerical simulations presented in Sect. 5.
3. We carry again an eigenvalue analysis of the stiffness matrix (3.6) associated to the N0M1S0-E and N0M1S0-LE elements of this section for the case of a fully opened hinge (i.e. $\boldsymbol{H} = 0$ in (3.8)). Both elements show three extra zero-energy modes in addition of the basic three rigid body modes, hence confirming the absence of stress locking for both elements. The component associated to the bubble in rotation ($\Delta\vartheta_{12}$) vanishes in particular. The N0M1S0-LE possesses the three exact modes as in (4.10), that is, the two pure opening in longitudinal and transversal directions, and the rotation about the plastic hinge at s_d. However, this last rotation mode is not reproduced exactly by the N0M1S0-E element, but with $h_e - s_d$ in (4.10) replaced by $h_e/2$. As observed in Remark 4.2.2, this element reproduces the zero strain mode for a hinge located at the center of the element, despite the actual location of the hinge at s_d. □

5 Representative numerical simulations

We present in this section several numerical examples involving the new enhanced finite elements developed

in this paper. The sole purpose of the discussion presented here is to evaluate and compare the numerical performance of the different finite elements. Section 5.1 considers a simple cantilever beam in combination with different interaction diagrams, illustrating the effects of stress-locking in this simple setting. Section 5.2 considers the problem of the push-over of a frame, involving the formation of a more involved pattern of plastic hinges.

5.1 Cantilever beam

The effects of stress locking in the performance of the different finite elements presented in Sect. 4 can be easily illustrated through a simple cantilever beam problem. We consider a cantilever beam of length $L = 1$ under a fixed imposed longitudinal displacement and an increasing transversal displacement at the free end. Seeking to avoid the well-known shear locking effects, we choose the material properties such that (GA_sL^2/EI) is small ($\ll \infty$), that is, far from the thin-beam limit where those effects are of major influence. In particular, the simulations presented here consider the elastic model (2.15) with elasticities $EA = 0.2$, $EI = 1$ and $GA_s = 0.641$. We note, however, that the N0M0S1 elements lock in shear in the thin-beam limit.

We consider four different interaction diagrams (or yield functions) separately to test the responses of the plastic hinge in pure bending, pure shear, coupled shear-bending response, and coupled axial-bending. No additional insights have been gained for the other possible couplings. Since our only goal is to test the numerical performance of the different elements, we consider the simple interaction diagrams

$$\tilde{\phi}_1(M_d, \tilde{q}) = \frac{|M_d|}{M_y} - (1 - \tilde{q}) \ , \tag{5.1}$$

$$\tilde{\phi}_2(V_d, \tilde{q}) = \frac{|V_d|}{V_y} - (1 - \tilde{q}) \ , \tag{5.2}$$

$$\tilde{\phi}_3(M_d, V_d, \tilde{q}) = \frac{|M_d|}{M_y} + \frac{|V_d|}{V_y} - (1 - \tilde{q}) \ , \tag{5.3}$$

$$\tilde{\phi}_4(N_d, M_d, \tilde{q}) = \frac{|N_d|}{N_y} + \frac{|M_d|}{M_y} - (1 - \tilde{q}) \ , \tag{5.4}$$

with yield limits $N_y = 1$, $M_y = 1$ and $V_y = 1$. In all cases, we consider the linear softening response

$$\tilde{q}(\tilde{\alpha}) = \min\{1, -\mathscr{H}\alpha\} \ , \tag{5.5}$$

with softening modulus $\mathscr{H} = -0.1$. We present next a detailed analysis illustrating the numerical performance of the different elements for these cases.

5.1.1 Pure bending interaction diagram

We start by considering the interaction diagram $\tilde{\phi}_1$ in (5.1) depending on the bending moment only. A transversal displacement is applied at the free end, leading to a linear bending distribution along the span of the beam. The solution is initially linear elastic until a plastic hinge on the rotation (that is, with ξ^{ϑ}) forms at the clamped end ($x = 0$) when the bending moment reaches the yield value $M_y = 1$. The bending moment at this end softens following the linear softening law (5.5) as additional transversal displacement is imposed, with the rest of the beam unloading elastically. The axial component does not affect the solution in this uncoupled case, with the axial response remaining elastic throughout for the fixed imposed longitudinal displacement. Hence, we do not consider it in the discussion that follows.

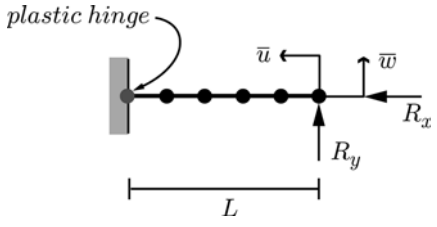

Fig. 5.1 Cantilever beam: problem definition. A cantilever beam of span L is subjected to an imposed transversal and/or longitudinal displacement at the free end ($\bar{w}$ and $\bar{u}$, respectively), measuring the corresponding reactions (R_y and R_x). A plastic hinge is activated at the fixed end

Figure 5.2 depicts the solution obtained with the N0M0S1-E, N0M0S1-LE, N0M1S0-E and N0M1S0-LE elements, while Fig. 5.3 shows the solution for the N0M0S0-E in this case. They include the evolution of the reacting transversal force versus the imposed transversal displacement, and the spatial distributions of the transverse shear force and the bending moment at the imposed displacement $\bar{w} = 6$, before the plastic hinge has fully softened. The discontinuous distributions of the stress resultants across elements are smoothed by considering the average values at the nodes. Equally spaced elements are considered in all the numerical simulations. Similar considerations apply to all the plots showing spatial distributions along the span in what follows.

The solution depicted in Fig. 5.2 for the N0M0S1-E element clearly shows the stress-locking that this element exhibits. The reaction increases even after the plastic hinge is formed, after an initial softening response. The locking is more severe for coarser meshes, eventually disappearing as the mesh is refined. As discussed in Sect.4, this element is not able to reproduce a fully softened state of strain (or stress) for a finite element length $h_e > 0$. A spurious transfer of bending moment occurs, leading to the over-stiff (even hardening) response of the element. The poor resolution of the transverse shear force and bending moment resolution obtained with the element, with unphysical oscillations in the former, can also be observed in Fig. 5.2.

This situation is to be contrasted with the results obtained with the linked enhancement for the same base finite element, that is, for the N0M0S1-LE element. The element does not show stress-locking, as verified by the absence of the stiffening of the softening response. Still

N0M0S1-E

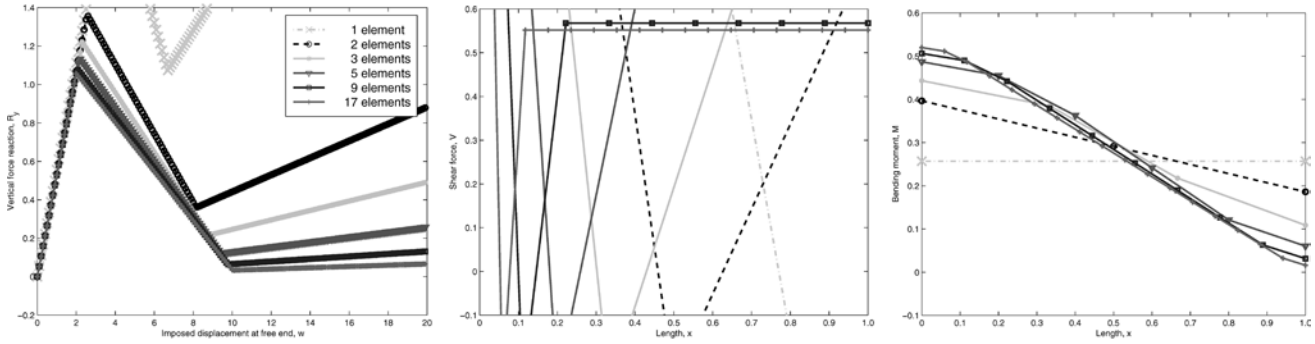

N0M0S1-LE

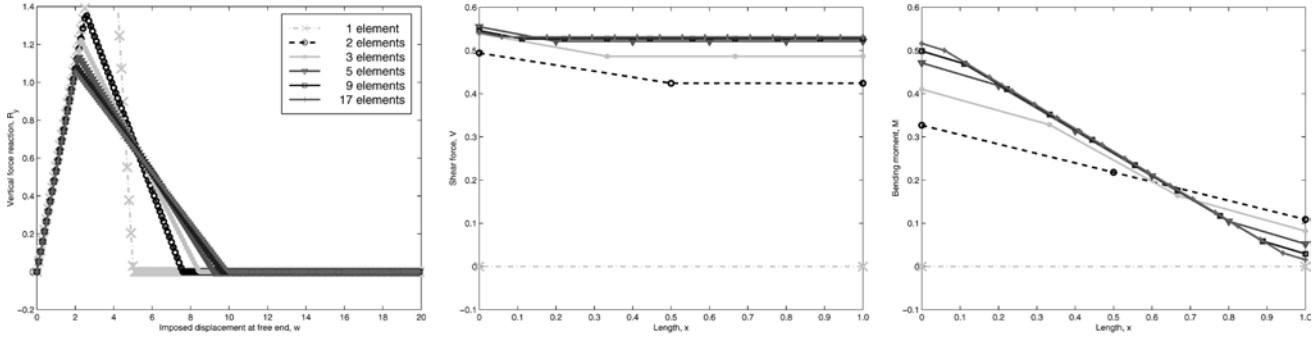

N0M1S0-E

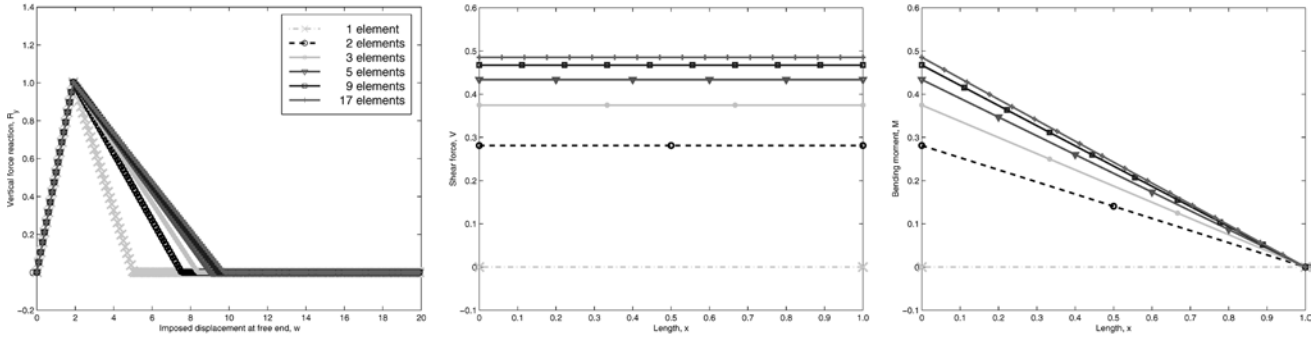

N0M1S0-LE

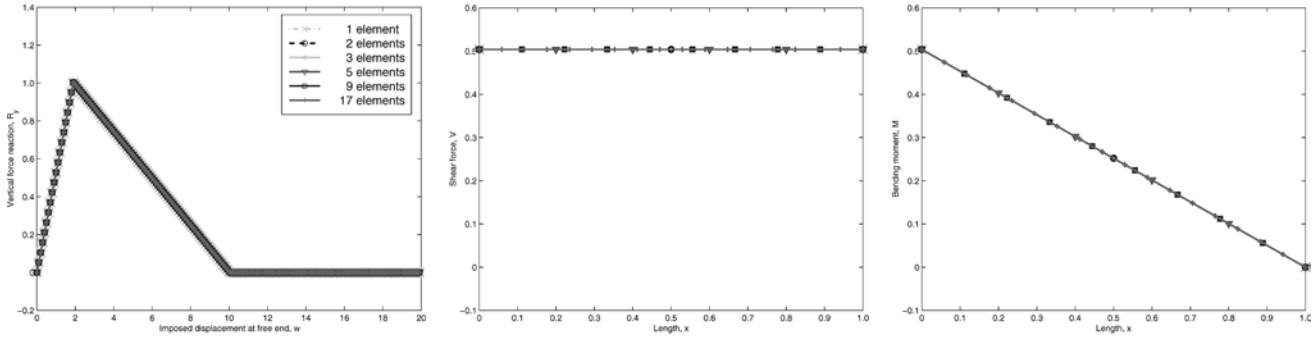

R_y *vs.* $\bar{w}$ $V(x)$ $(\bar{w} = 6)$ $M(x)$ $(\bar{w} = 6)$

◀

Fig. 5.2 Cantilever beam with imposed transversal displacement. Solutions for a plastic hinge in bending ($\tilde{\phi}_1$ interaction diagram): transversal reacting force vs. imposed displacement, and the distribution along the span x of the transverse shear force and bending moment at imposed displacement $\bar{w} = 6$. All plots follow the same legend

we can observe a much stiffer response for coarse meshes, especially in the limit load. Convergence occurs as the meshes are refined. These considerations are also apparent in the distributions of the transverse shear force and bending moment shown in Fig. 5.2 for different meshes. A similar performance can be observed for the constant strain element N0M0S0-E in Fig. 5.3.

Figure 5.2 shows also the solution for the linear moment elements N0M1S0-E and N0M1S0-LE. Both elements coincide in the elastic range, capturing exactly the limit load. As argued in Remark 4.2.1, no stress-locking is to be observed for either element, but the N0M1S0-E is not able to capture the exact solution. The discrepancy is apparent for coarse meshes, diminishing as the mesh is refined. We refer to Remark 4.2.1 for an analytical explanation of this response. In contrast, the N0M1S0-LE is able to capture the exact solution for any mesh in this case with linear bending moment and constant transverse shear force. This includes not only the evolution of the reacting force versus imposed transversal displacement, but also the spatial distributions of the transverse shear force and the bending moment. This property is to be traced to the correct resolution of the hinge mode by the enhanced element in these conditions.

5.1.2 Pure transverse shear interaction diagram

Figure 5.4 depicts the solutions obtained for the interaction diagram in the transverse shear $\tilde{\phi}_2$ in (5.2). Once again the exact constant linear elastic axial response is reproduced exactly by all the elements and its consideration is omitted in the following discussion. The exact solution consists of an initial elastic phase with constant transverse shear force and linear distribution of bending moment. When the transverse shear force reaches the yield value $V_y = 1$ a hinge is formed, consisting of a jump in the deflection ξ^w. In order to break the symmetry, and trigger the formation of the plastic hinge at the clamped end, an imperfection (lower V_y) is considered in the first element from the fixed support. Under the increasing imposed transversal deflection, the shear hinge softens following the assumed linear softening law (5.5), with the rest of the beam unloading elastically.

The same response is to be expected in this case for the non-linked and linked enhanced elements (i.e., -E and -LE elements), due to the absence of a jump in the rotation ξ^ϑ. In particular, no stress-locking is to be expected for the -E elements. These observations are confirmed by the numerical simulations. Figure 5.4 shows again the evolution of the transversal reacting force versus the imposed transversal displacement, and the spatial distributions of the transversal shear force and the bending moment at the imposed displacement $\bar{w} = 6$, before the plastic hinge fully softens. Different meshes with equally spaced finite elements are again considered.

We can observe how again the N0M0S1 and N0M0S0 based elements are not capable of reproducing the constant transverse shear and linear bending moment distributions exactly. Different responses are obtained for different meshes, converging eventually to the exact solution as the mesh is refined. In contrast, the N0M1S0 based elements are able to capture the exact solution for any mesh in this case.

5.1.3 Coupled transverse shear-bending interaction diagram

We consider next the yield surface $\tilde{\phi}_3$ in (5.3) involving a coupled response of the transversal shear and bending moment at the plastic hinge. The axial response remains

Fig. 5.3 Cantilever beam with imposed transversal displacement. Solutions for a plastic hinge in bending ($\tilde{\phi}_1$ interaction diagram): transversal reacting force vs. imposed displacement, and the distribution along the span x of the transverse shear force and bending moment at imposed displacement $\bar{w} = 6$. All plots follow the same legend

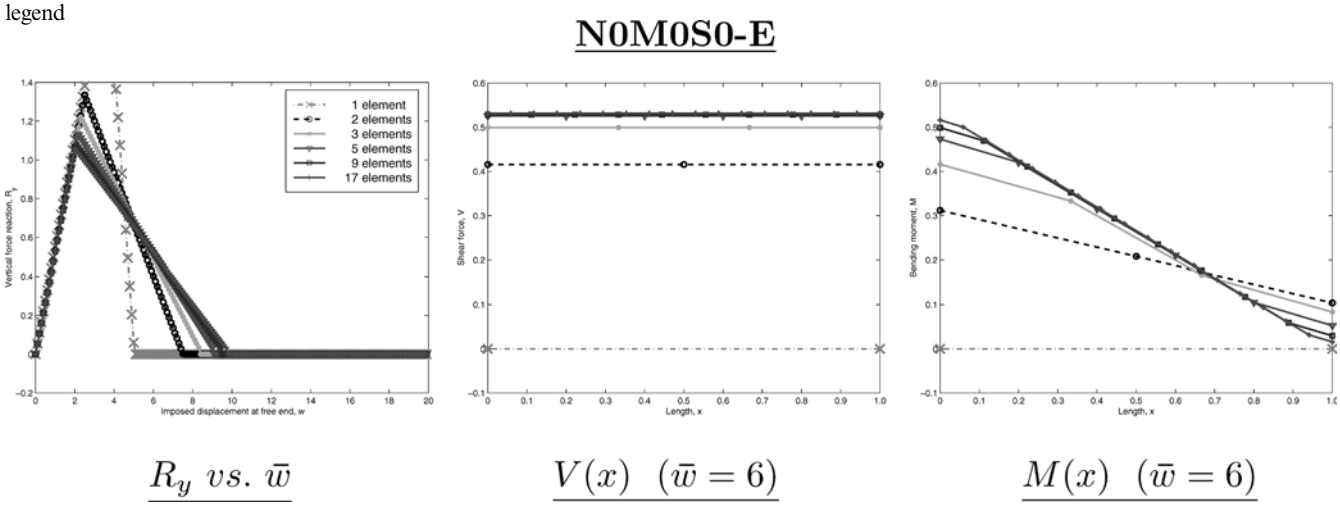

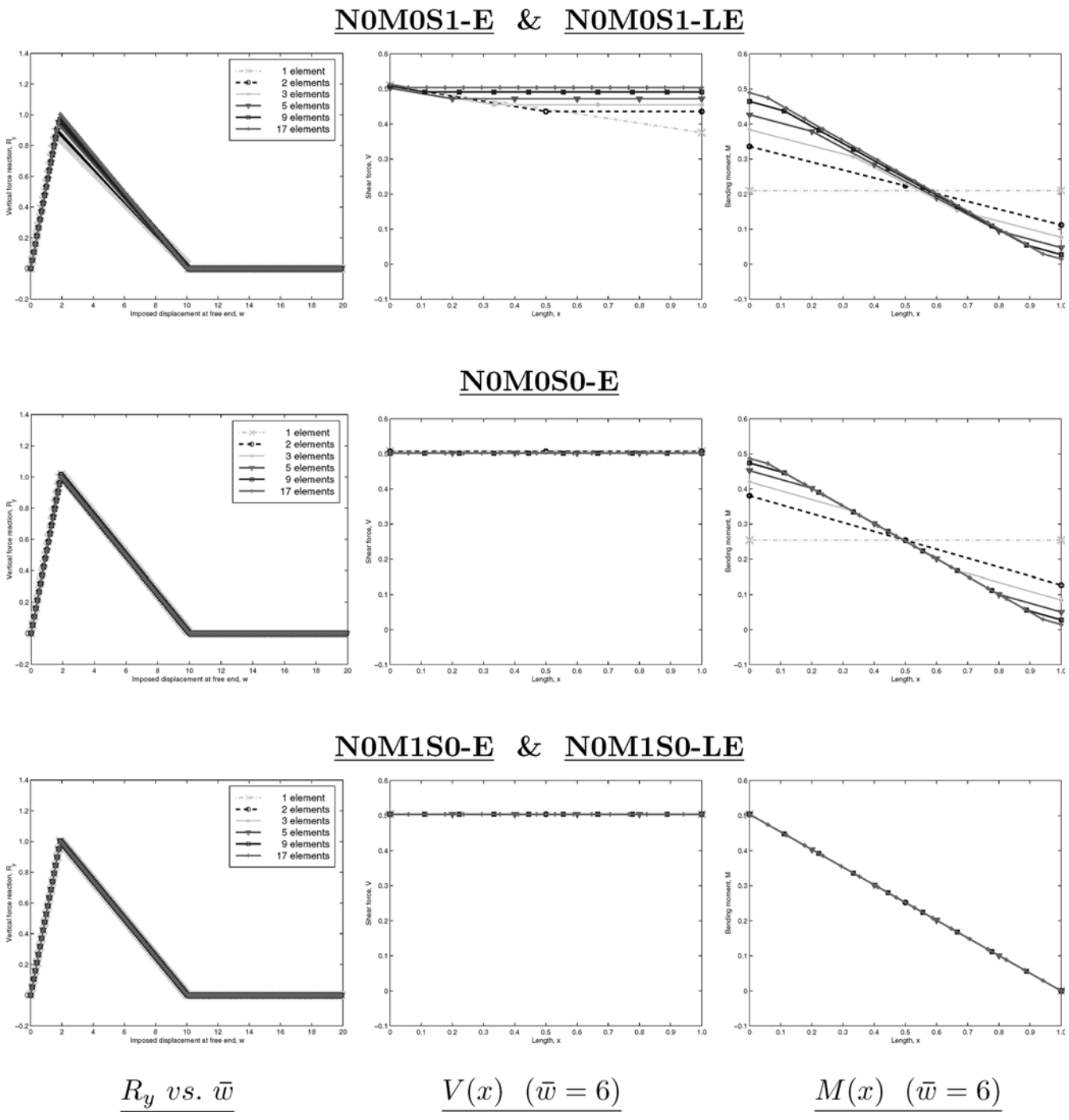

Fig. 5.4 Cantilever beam with imposed transversal displacement. Solutions for a plastic shear hinge ($\tilde{\phi}_2$ interaction diagram): transversal reacting force vs. imposed displacement, and the distribution along the span x of the transverse shear force and bending moment at imposed displacement $\bar{w} = 6$. All plots follow the same legend

elastic and so it is again ignored in the discussion that follows. After the initial linear elastic response, a plastic hinge is formed at the clamped end of the cantilever when the stress-resultants at this point reach the values $(M(0), V(0)) = (0.5, 0.5)$ for the assumed material parameters (note that by simple equilibrium $M(0) = V(0)L$ for $L = 1$ even in the plastic range). A plastic hinge forms then at the clamped end involving the transversal displacement jump ξ^w and a rotation jump ξ^ϑ. Given the assumed normality of the plastic response by the evolution Eq. (2.12), the direction of the plastic jump vector (ξ^w, ξ^ϑ) is orthogonal to the yield surface. In fact, given the constant relation between $M(0) = V(0)L$ and the assumed piece-wise linear interaction diagram, this direction remains constant as the elastic domain softens for the increasing imposed transversal displacement.

Figure 5.5 depicts the solution obtained with the N0M0S1-E, N0M0S1-LE, N0M1S0-E and N0M1S0-

N0M0S1-E

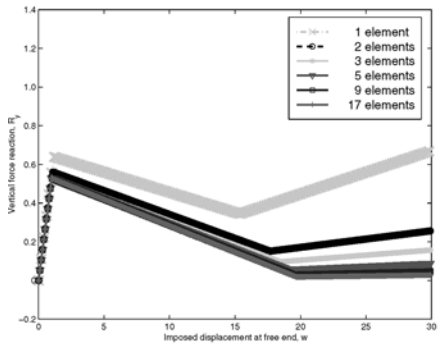

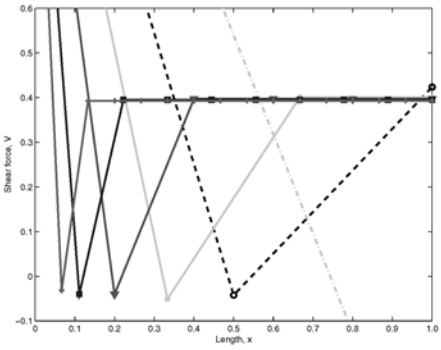

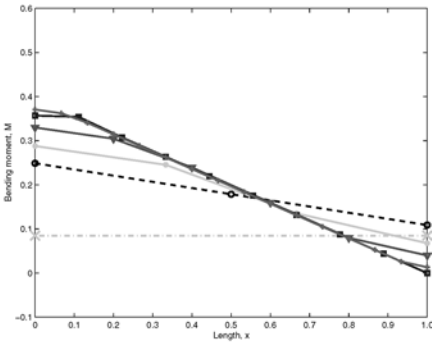

N0M0S1-LE

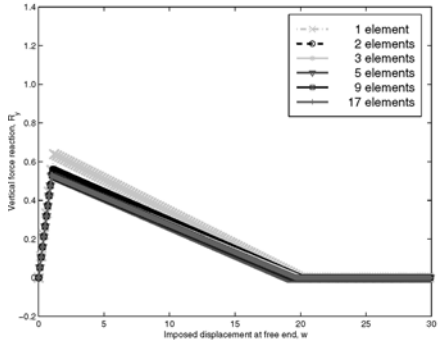

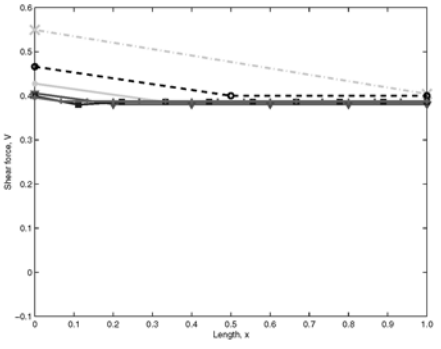

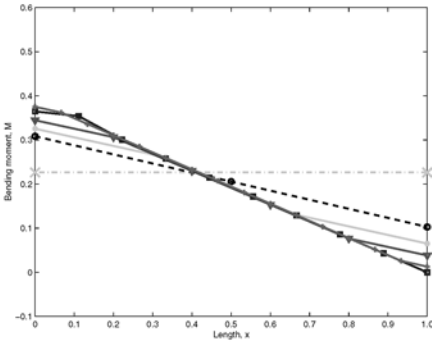

N0M1S0-E

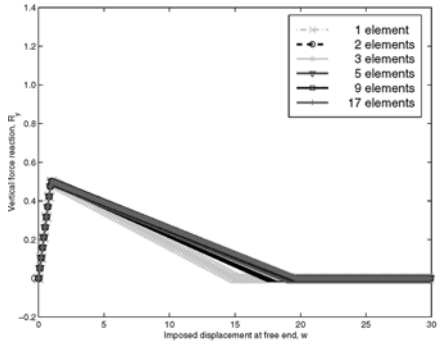

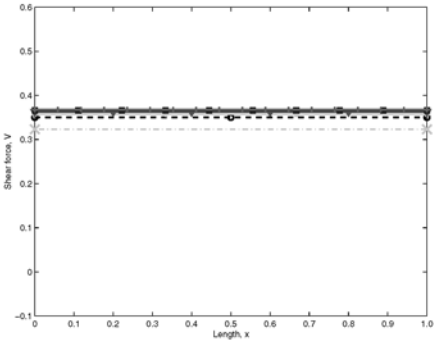

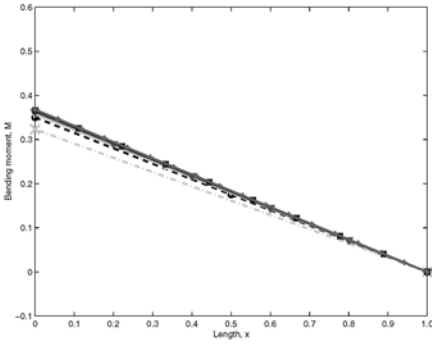

N0M1S0-LE

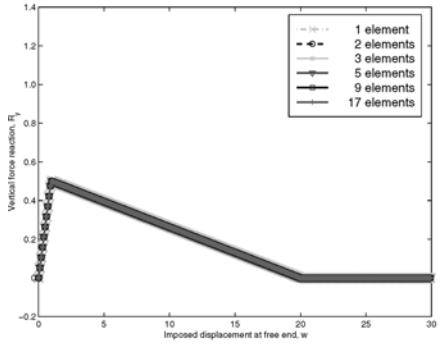

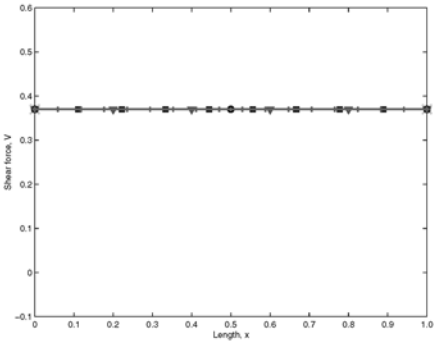

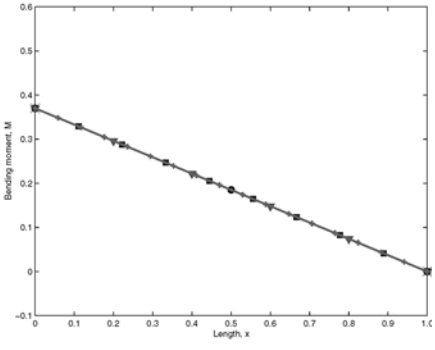

$R_y \; vs. \; \bar{w}$ $\quad$ $V(x) \;\; (\bar{w} = 6)$ $\quad$ $M(x) \;\; (\bar{w} = 6)$

◄

Fig. 5.5 Cantilever beam with imposed transversal displacement. Solutions for a plastic hinge in bending and transverse shear ($\tilde{\phi}_3$ interaction diagram): transversal reacting force vs. imposed displacement, and the distribution along the span x of the transverse shear force and bending moment at imposed displacement $\bar{w} = 6$. All plots follow the same legend

LE elements, while Fig. 5.6 depicts the solution for the constant strain N0M0S0-E element. The evolution of the reacting transversal force versus the imposed transversal displacement, and the spatial distributions of the transverse shear force and the bending moment are again shown at $\bar{w} = 6$, before the plastic hinge fully softens, for different equally spaced finite element meshes.

The same qualitative response as in the case of a plastic hinge in pure bending discussed in Sect. 5.1.1 can be observed. In particular the severe stress locking of the N0M0S1-E element is again clear, being eliminated by the linked enhancement LE. The exact solution is again recovered for any mesh with the N0M1S0-LE element, thanks to the correct resolution of the kinematics of the hinge mode.

5.1.4 Coupled axial-bending interaction diagram

We consider in this section the case defined by the interaction diagram $\tilde{\phi}_4$ in (5.4) depending of the axial force and the bending moment. The influence of the axial force will now affect the results. We consider an imposed longitudinal displacement $\bar{u} = 2.5$, kept fixed during the entire simulation, while the imposed transversal displacement $\bar{w}$ is increased linearly to load the cantilever. In this case, the initial response is linear elastic until the stress resultants reach the yield surface at the point $(N, M) = (0.5, 0.5)$ in stress space at the clamped end of the cantilever. A plastic hinge involving a longitudinal displacement jump ξ^u and a rotation jump ξ^ϑ is formed at this point. The increasing imposed transversal displacement leads to the softening of the hinge. The direction of the plastic jump vector (ξ^u, ξ^ϑ) is orthogonal to the yield surface $\tilde{\phi}_4$. Both components of the jump vector increase for additional imposed transversal displacement, resulting in an unloading of the axial force and a smaller stiffness in the bending response, until the axial force is fully unloaded. This occurs when the stress resultants reach a vertex of the yield surface. The longitudinal displacement jump ξ^u then ceases to evolve. Afterwards, the response of the plastic hinge consists of a softening of the bending response, leading to a decrease of the moment (and reacting transversal force) for increasing imposed transverse displacement, with an elastic unloading elsewhere in the beam.

Figures 5.7 and 5.8 depict the solution obtained with the N0M0S1-E, N0M0S1-LE, N0M1S0-E and N0M1S0-LE elements in this case, while Fig.5.9 shows the solution for the constant strain N0M0S0-E element. We show in all these figures the evolution of the reacting transversal and longitudinal forces versus the imposed transversal displacement, a transversal force versus horizontal force diagram, and the distributions of the axial force, the transverse shear force and the bending moment at the imposed transversal displacement $\bar{w} = 3$. The discontinuous distributions of the stress resultants across elements are again smoothed by considering the average values at the nodes. Equally spaced elements are considered.

The different features of the solution outlined above can be observed in these solutions. Note the change of the slope (stiffness) in the evolution of the transversal reaction versus imposed displacements corresponding to the formation of the plastic hinge at the fixed end. The axial force starts then decreasing whereas the reacting transversal force (and reacting bending moment $M(0) = R_y L$) keeps increasing. This situation is clearly

Fig. 5.6 Cantilever beam with imposed transversal displacement. Solutions for a plastic hinge in bending and transverse shear ($\tilde{\phi}_3$ interaction diagram): transversal reacting force vs. imposed displacement, and the distribution along the span x of the transverse shear force and bending moment at imposed displacement $\bar{w} = 6$. All plots follow the same legend

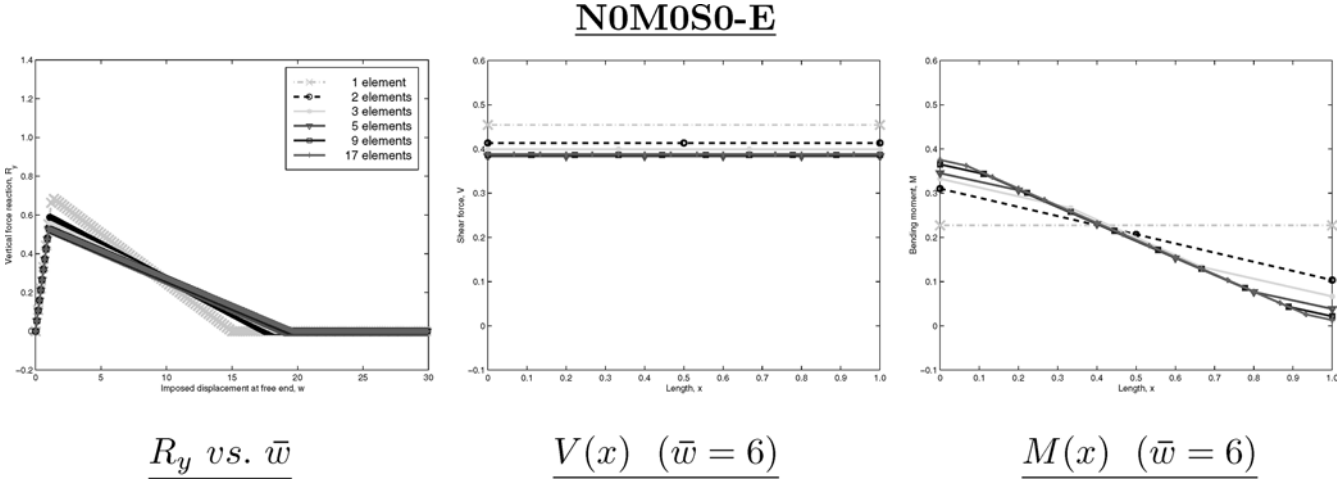

N0M0S1-E

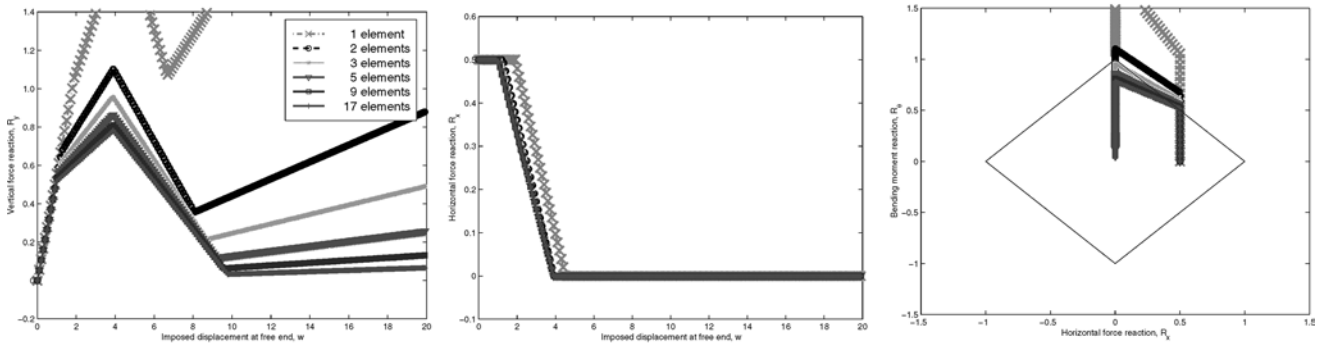

N0M0S1-LE

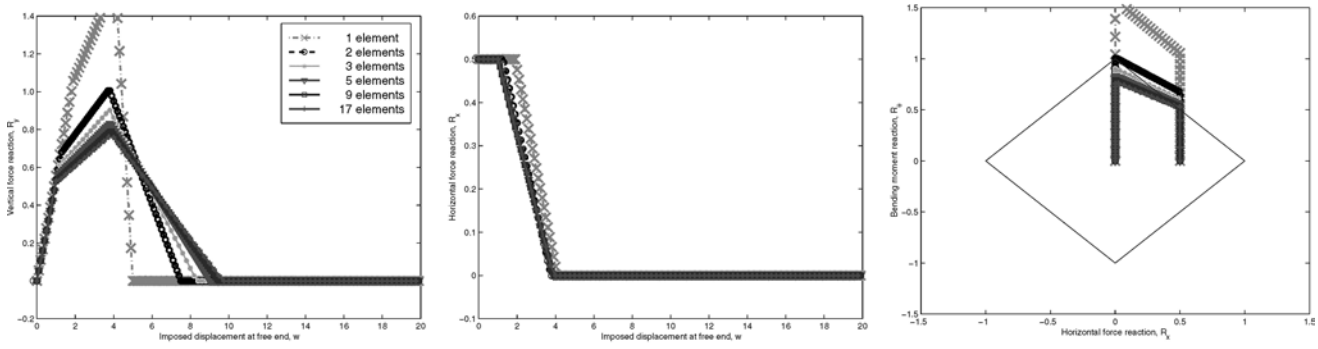

N0M1S0-E

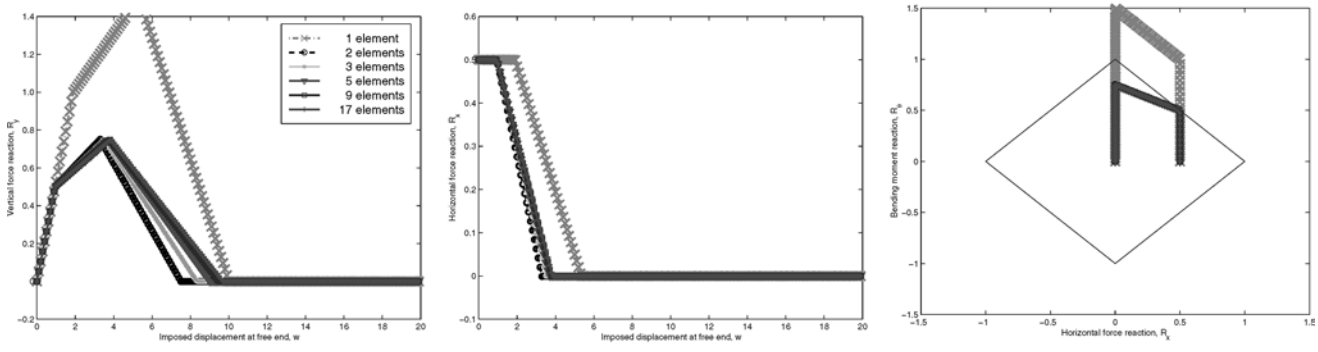

N0M1S0-LE

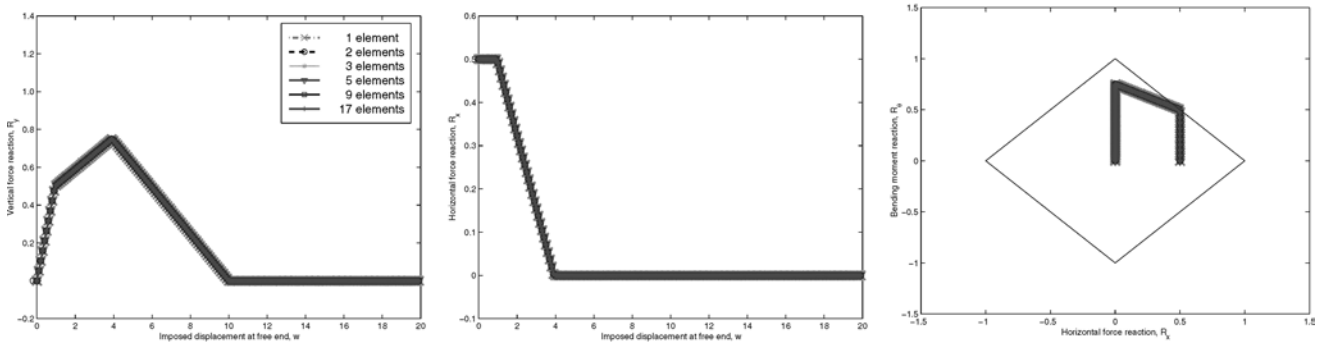

R_y *vs.* $\bar{w}$ R_x *vs.* $\bar{w}$ R_y *vs.* R_x

◀

Fig. 5.7 Cantilever beam with imposed longitudinal and transversal displacements. Solutions for a plastic hinge in axial force and bending ($\tilde{\phi}_4$ interaction diagram): transversal and longitudinal reacting forces vs. imposed displacement, and transversal vs. longitudinal reacting force. All plots follow the same legend

depicted in the diagrams of the reacting bending moment and longitudinal force of Fig. 5.7 and 5.9. The overall reduction of the size of the elastic domain due to the softening is apparent. The decrease of the reacting bending moment starts when the axial force has soften completely.

Once again the stress locking of the element N0M0S1-E is clearly noticeable. The over-stiff response is less marked as the mesh is refined. Adding the linked enhancement in the N0M0S1-LE element eliminates this stiffening of the softening response. However, for coarse meshes the response is still stiff, with considerable overestimation of the limit load. Convergence occurs as the meshes are refined. Similar performance can be observed for the constant strain element N0M0S0-E in Fig. 5.9. Stress locking is not observed for the N0M1S0-E and N0M1S0-LE elements, but the N0M1S0-E element is not able to capture the exact response except for the limit $h_e \to 0$. The differences are apparent for coarse meshes. The exact solution is recovered for the N0M1S0-LE element for any mesh.

5.2 Push-over of a frame

We consider next the more involved example of the push-over of a frame. In particular, we study the failure of the two story frame depicted in Fig. 5.10. The frame is loaded in two phases. Initially, two transversal forces of value $P = 100$ kips are applied at the center of the beams and kept constant. They are followed by imposed horizontal displacements at nodes A and B (see Fig. 5.10 in 100 increments of 0.05 inches each.

The localized plastic model (2.12) is considered again, with the coupled axial-bending interaction diagram $\tilde{\phi}_4$, defined in (5.4). We consider again the simple setting of a linear elastic response followed by the localized softening law (5.5) with softening modulus $\mathscr{H} = -0.001$ kip-in. The plastic hinges are then activated upon yielding. More involved hardening/softening laws can be considered to arrive to a more realistic response involving an initial spread of bulk plasticity. However, our goal here is again the evaluation of the finite elements in the resolution of the plastic hinges. Similarly, the simulations presented here do not involve the corner of the yield surface (5.4), requiring a multi-surface form of Eq. (2.12) and their special numerical integration. As noted above, we plan to address these issues in a separate article.

We also consider numerical simulations based on the continuum model (2.6). The same yield surface (5.4), now in terms of the point value of the bending moment M and axial force N, is also considered. A linear strain softening law is again considered with (continuum) softening modulus $\mathscr{H}_{\text{cont}} = -0.036$ kips. The constant strain N0M0S0 element, leading to a Galerkin approximation of the inelastic problem, is considered for this continuum model.

Figure 5.11 depicts the horizontal reacting force at node A for the N0M0S0 element with the continuum model and for the N0M0S0-E and N0M1S0-LE enhanced elements with the localized model (2.12). The pathological mesh-size dependence of the Galerkin solution based on the continuum model is apparent. A significantly softer response is observed as the mesh is refined, leading eventually to an unphysical solution exhibiting no energy dissipation. This situation confirms the analyses presented in Armero & Ehrlich [2002] identifying the ill-posedness of problem based on the continuum model despite the presence of a length scale in the problem (namely, the thickness). These difficulties are completely avoided by the localized model, leading to numerical solution converging to a physically meaningful (dissipative) solution.

The two considered enhanced elements for the localized model, the N0M0S0-E and N0M1S0-LE elements, show no shear nor stress locking. The much superior performance of the N0M1S0-LE element observed in the different tests of the previous section is also clearly manifested in this example. The element is able to capture again the exact solution in this case involving no distributed loads, but only point loads at the nodes. We observe that this property is not only a direct consequence of the piece-wise linear character of the stress resultant distributions at the element level, but also of the correct resolution of the kinematics of the plastic hinges by the newly proposed N0M1S0-LE enhanced element. The crucial need of the specific linked enhancement developed in Sect. 4.4 is to be noted to arrive to this result.

Figure 5.10 depicts also the deformed configuration of the frame obtained with the N0M1S0-LE enhanced element at an imposed displacement of $\bar{u} = 5$. Several plastic hinges form during the loading process. They are depicted superposed to the deformed configuration in Fig. 5.10 with a number indicating the order of their formation. Figure 5.12 depicts the evolution of the equivalent plastic jump $\tilde{\alpha}$ in the localized plastic model (2.12) for the different hinges. A complex pattern of plastic hinge formation and interaction is observed, leading to the redistribution of the stress resultants throughout the structure. In particular, some of the plastic hinges become deactivated during the loading process.

6 Concluding remarks

We have presented in this paper a general framework for the characterization of plastic hinges in beams/rods.

N0M0S1-E

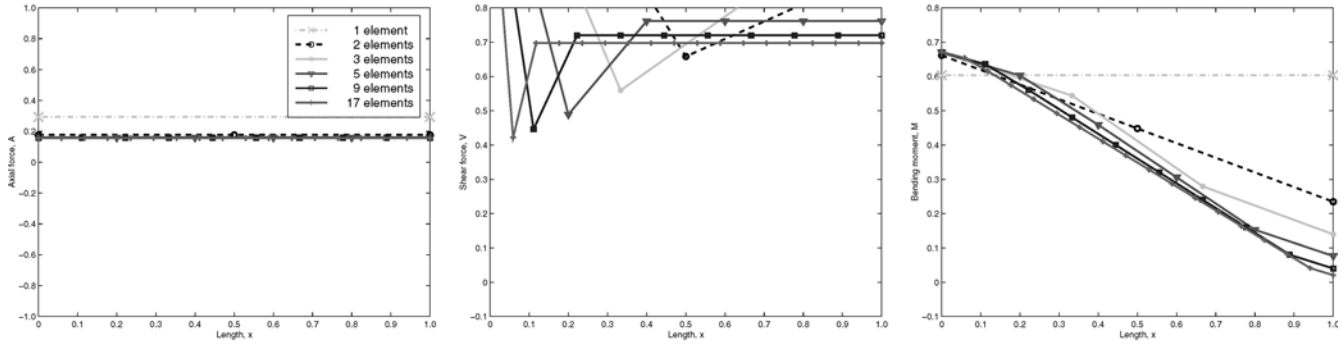

N0M0S1-LE

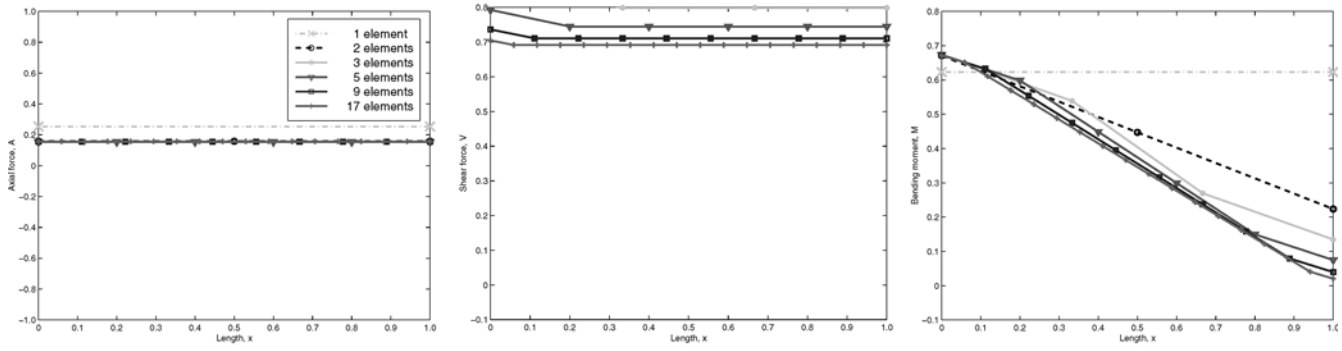

N0M1S0-E

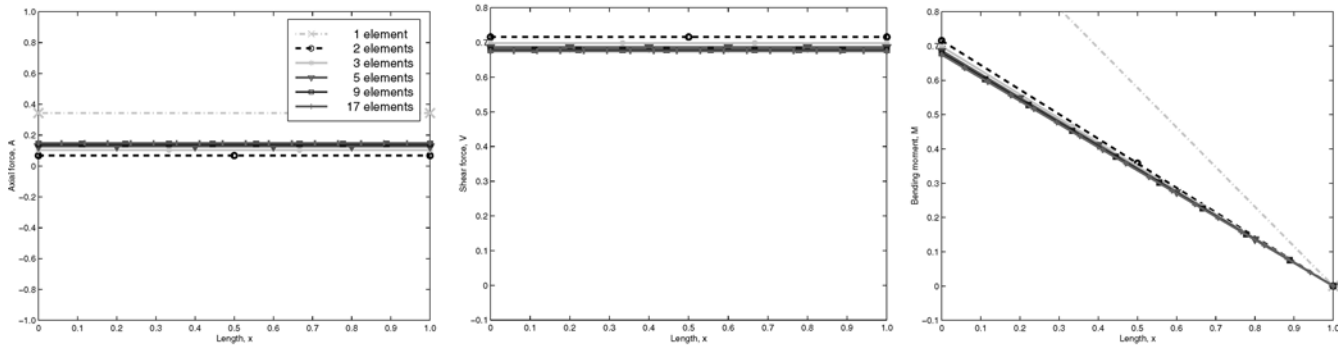

N0M1S0-LE

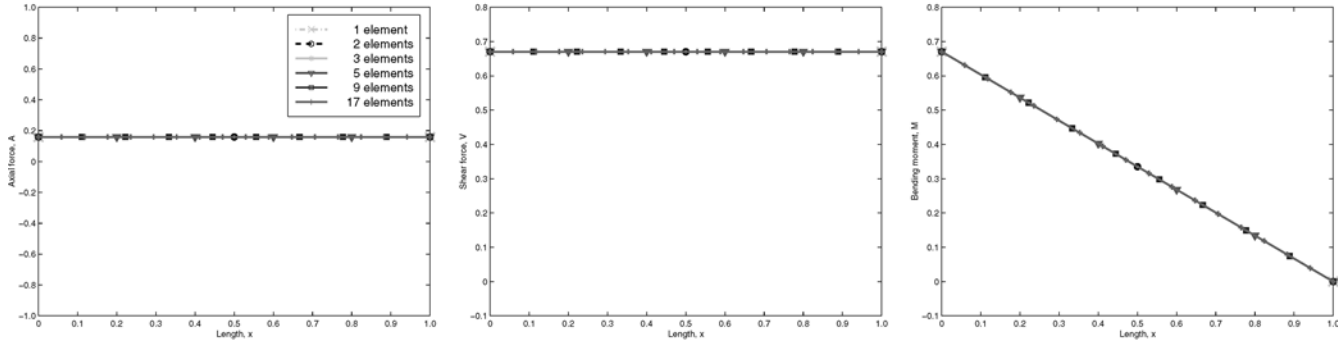

$N(x) \quad (\bar{w} = 3)$ $V(x) \quad (\bar{w} = 3)$ $M(x) \quad (\bar{w} = 3)$

◄

Fig. 5.8 Cantilever beam with imposed longitudinal and transversal displacements. Solutions for a plastic hinge in axial force and bending ($\tilde{\phi}_4$ interaction diagram): distribution along the span x of the axial force, transverse shear force and bending moment at imposed displacement $\bar{w} = 3$. All plots follow the same legend

The considered formulation falls within the so-called strong discontinuity approach: the plastic hinges correspond to discontinuities of the generalized displacement fields of the underlying Timoshenko theory. We have developed in this context what we refer as localized models, incorporating the localized effects associated with the plastic hinges. This is accomplished, in particular, in a multi-scale framework avoiding the explicit consideration of small scales in the large-scale problem of the beams and general frames of interest here, while effectively incorporating the localized dissipative effects of the plastic hinges in this problem. The resulting localized models maintain the structure of the typical large-scale structural problem, while capturing the dissipative mechanisms characteristic of the localized failures of structural systems.

Fig. 5.9 Cantilever beam with imposed longitudinal and transversal displacements. Solutions for a plastic hinge in axial force and bending ($\tilde{\phi}_4$ interaction diagram): First row: transversal and longitudinal reacting force vs. imposed displacement, and transversal vs. longitudinal reacting force. Second row: distribution along the span x of the axial force, transverse shear force and bending moment at imposed displacement $\bar{w} = 3$. All plots follow the same legend

The constructive approach considered in the development of these models has naturally led to the formulation of enhanced finite element methods for their numerical simulation, the main goal of the current cpaper. We have presented several finite elements in this framework. A careful analysis of the kinematics of the beam/rod under consideration has led, in particular, to new enhancement strategies that avoid stress-locking. The coupling of the deflection and rotation fields in the definition of the strain measures defining the response of the beam/rod requires a similar linked character of the enhanced strains measures. Due to this more involved kinematics, the newly proposed finite elements are then not direct extensions of previously proposed enhanced finite elements for the resolution of strong discontinuities in continuum problems.

The resulting enhanced finite elements are able to accurately resolve the kinematics of the plastic hinges,

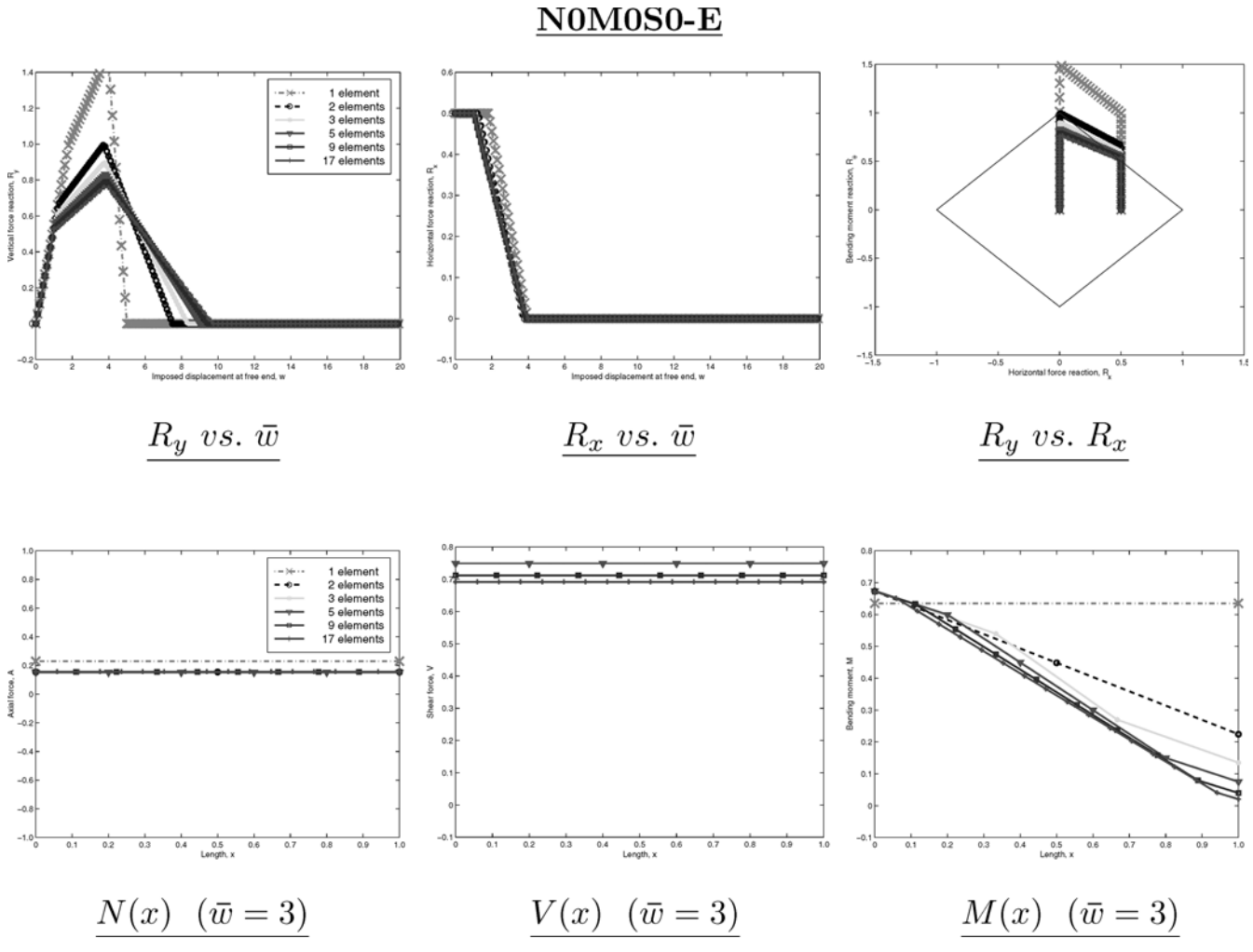

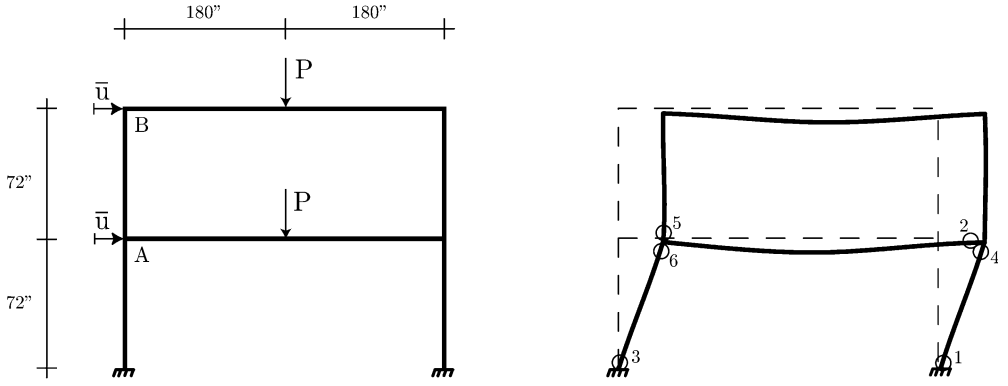

Fig. 5.10 Push-over of a frame: initial and deformed configurations. The loading consists of an imposed equal horizontal displacements at nodes A and B after two transversal forces have been applied at the center of the beams. The plastic hinges are shown in the deformed configuration, with the numbers indicating the order of appearance

Table 5.1 Push-over of a frame. Material properties.

Property	Beams	Columns
EA (kips)	$6.467 \cdot 10^5$	$7.685 \cdot 10^5$
GAs (kips)	$2.072 \cdot 10^5$	$2.463 \cdot 10^5$
EI (kips-in^2)	$3.875 \cdot 10^7$	$2.897 \cdot 10^7$
N_y (kips)	$1.115 \cdot 10^3$	$1.350 \cdot 10^3$
M_y (kips-in)	$7.300 \cdot 10^3$	$7.850 \cdot 10^3$

locally at the element level, leading to computationally very efficient formulations for the analysis of the failure of structural frames. The numerical performance of the proposed methods has been illustrated with a series of representative numerical simulations. We are currently extending these results to consider alternative models of the plastic response of the structural members of interest (e.g., fiber-based models). Similar, but more involved, enhanced strategies at both the constitutive and finite element levels can be considered to model the formation of hinge lines in plates and shells, as we plan to address in a forthcoming publication.

Appendix I

Approximations to the local equilibrium equation

The developments in Sect. (3.1) consider a special enhanced strain operator $\boldsymbol{G}_e$ in the discrete local equilibrium $(3.2)_2$ that enforces exactly the relation $\boldsymbol{\sigma}_d = \boldsymbol{\sigma}(s_d)$ for the driving stress resultant and the actual stress resultant, respectively, on the plastic hinge at s_d. The case of an at most linear distribution of the stress resultant $\boldsymbol{\sigma}(s)$, as it is the case for the finite elements considered in Sect. 4, was considered in the particular expression (3.4).

These considerations are a particular case of the following general result: for any integer n, there exist a function $g_n(s)$ such that

$$\frac{1}{h}\int_0^h g_n(s)\sigma_n(s)\mathrm{d}s = \sigma_n(s_d) \ , \tag{I.1}$$

for $s_d \in [0,h]$, with $h > 0$, and for all $\sigma_n(s)_n([0,h]) := \{\text{polynomials of degree } n \text{ in } [0,h]\}$.

Indeed, let $\{p_i(s)\}$, $i = 1,2,\ldots,n$ be a polynomial basis for $P_n([0,h])$. We then write $g_n(s)$ and $\sigma_n(s)$ as

$$g_n(s) = \sum_{j=1}^{n} b_j p_j(s) \quad \text{and} \quad \sigma_n(s) = \sum_{i=1}^{n} c_i p_i(s) \ . \tag{I.2}$$

in this basis. Introducing (I.2) in (I.1) we obtain

$$\sum_{i=1}^{n}\sum_{j=1}^{n} b_i c_j M_{ij} = \sum_{j=1}^{n} c_j p_j(s_d) \ , \tag{I.3}$$

where M_{ij} is the symmetric positive definite Gramm matrix

$$M_{ij} = \frac{1}{h}\int_0^h p_i(s)p_j(s)\mathrm{d}s \ , \tag{I.4}$$

associated to the polynomial basis $\{p_i(s)\}$. Given the arbitrariness of $\sigma_n(s)$ (i.e., c_j) in (I.3), we obtain

$$\sum_{i=1}^{n} b_i M_{ij} = p_j(s_d) \ . \tag{I.5}$$

for $j = 1,2,\ldots,n$. Equation (I.5) defines a symmetric (positive-definite) algebraic system of equations whose solution uniquely determines $\{b_j\}$ and, thus, $g_n(s)$.

Furthermore, given any smooth function $\sigma(s) : [0,h] \to \mathbb{R}$, we can write

$$\sigma(s) = \sigma_n(s) + o(h^{n+1}) \tag{I.6}$$

for a polynomial $\sigma_n(s)$ of degree n. The result (I.1) then implies

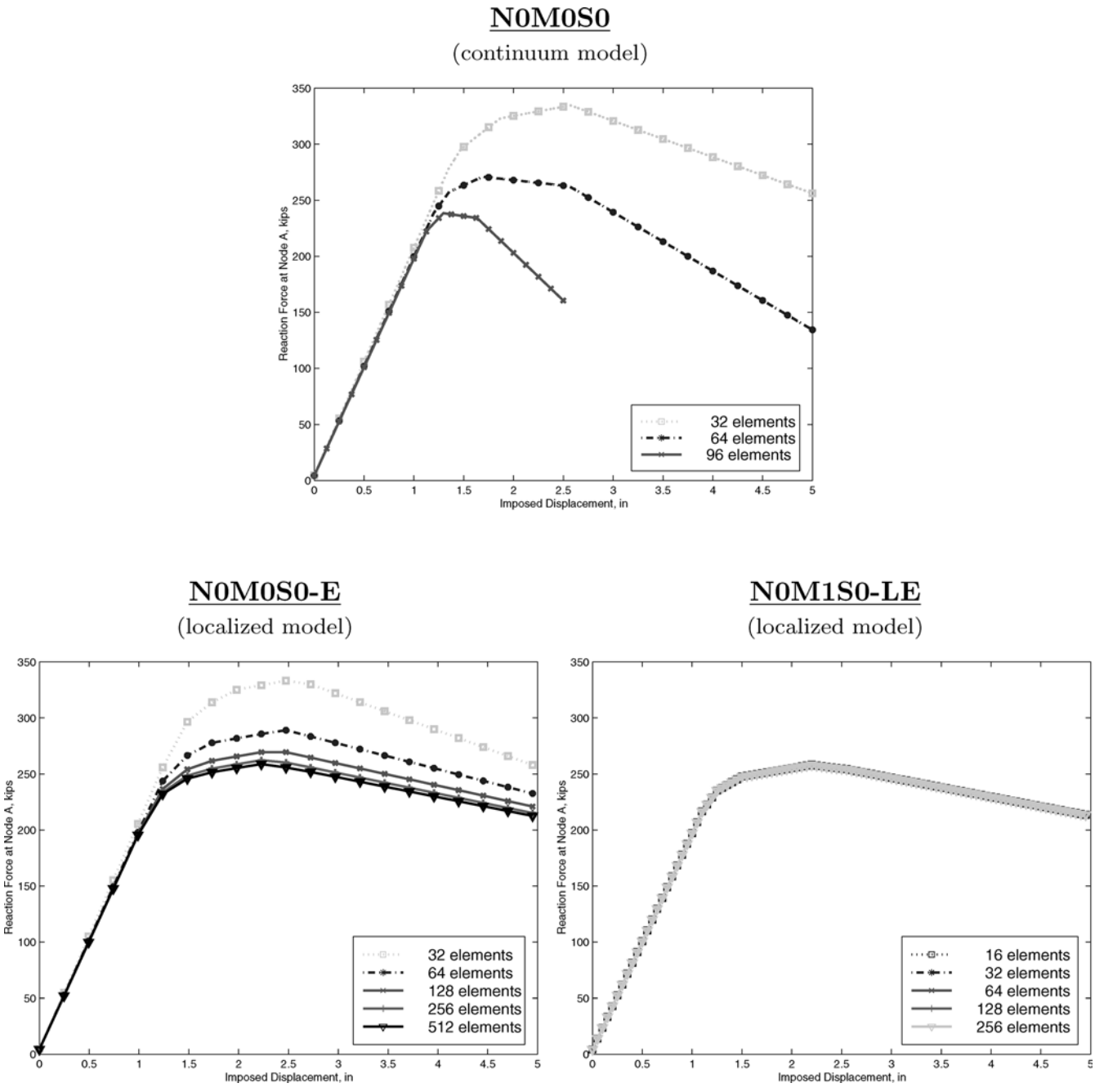

Fig. 5.11 Push-over of a frame: reacting force at node A versus imposed displacement. Solutions for the continuum model with the N0M0S0 element, and the localized model with the N0M0S0-E and N0M01S0-LE enhanced elements for different meshes. The number of elements in the legend is the total number of elements in the frame, with the same number of elements for each beam and column

$$\begin{aligned}\frac{1}{h}\int_0^h g_n(s)\sigma(s)\mathrm{d}x &= \frac{1}{h}\int_0^h g_n(s)\big(\sigma_n(s)+o(h^{n+1})\big)\mathrm{d}s\\ &= \sigma(s_d)+\left(\frac{1}{h}\int_0^h g_n(s)\mathrm{d}s\right)o(h^{n+1})\\ &= \sigma(s_d)+o(h^{n+1})\end{aligned} \tag{I.7}$$

since $g_n(s)$ is a polynomial in s.

The following cases are particular cases of these considerations:

1. $n = 0$. Then $p(s) = 1$ and (I.5) reduces to

$$b_1 = 1 \quad \text{so} \quad g_0(s) = 1\ . \tag{I.8}$$

2. $n = 1$. Let the elements of the polynomial basis be

$$p_0(s) = 1 \quad \text{and} \quad p_1(s) = s - \frac{h}{2}\ , \tag{I.9}$$

the Legendre polynomials in $[0, h]$. Then M_{ij} is diagonal, and (I.5) yields

$$b_0 = 1 \quad \text{and} \quad b_1 = \frac{12}{h^2}\left(s_d - \frac{h}{2}\right)\ , \tag{I.10}$$

Hinge #1

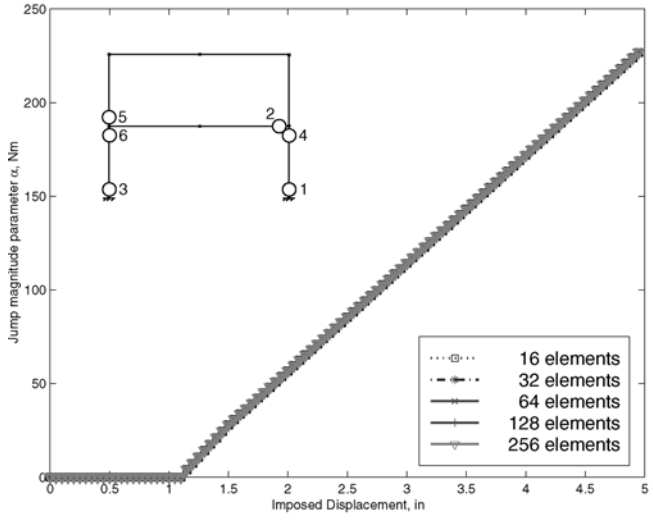

Hinge #2

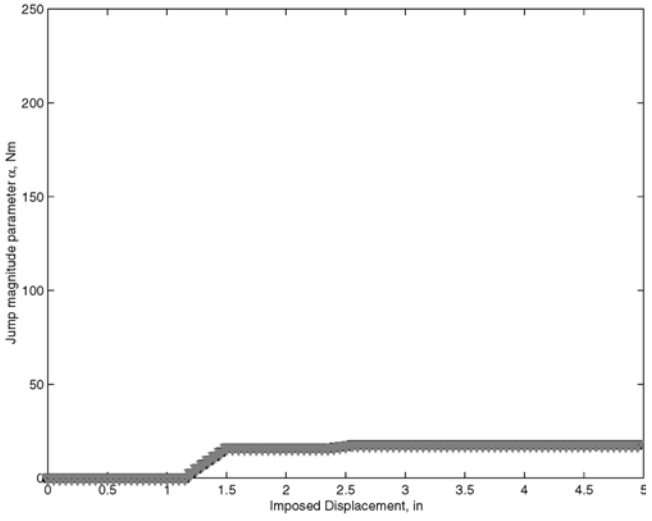

Hinge #3

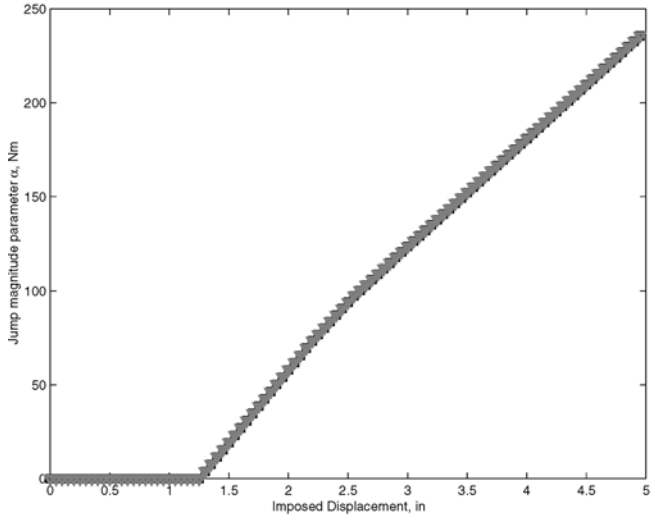

Hinge #4

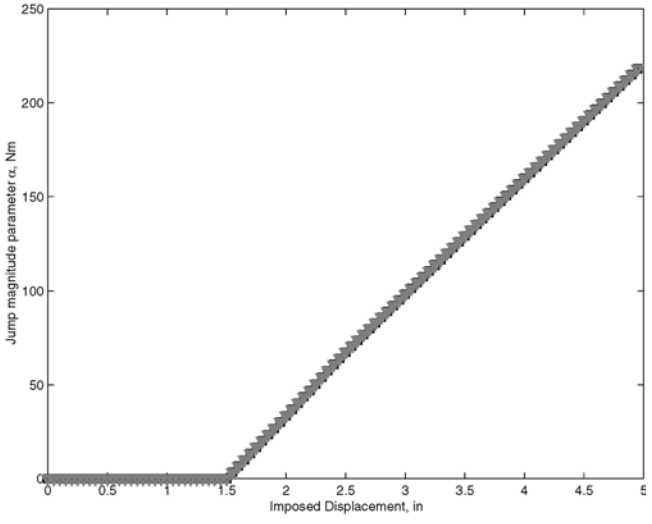

Hinge #5

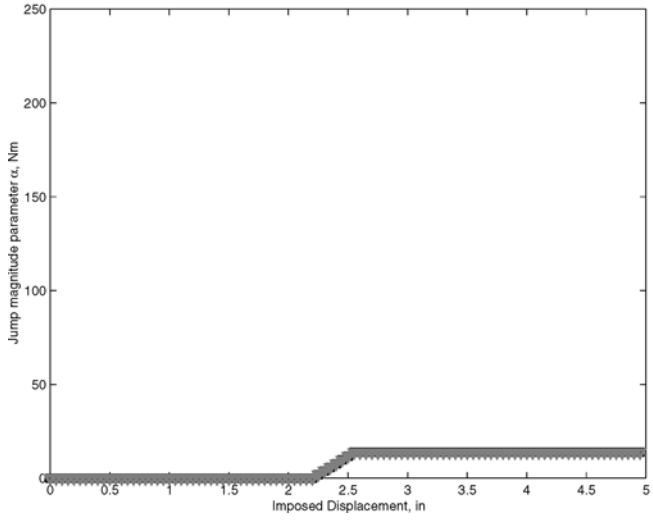

Hinge #6

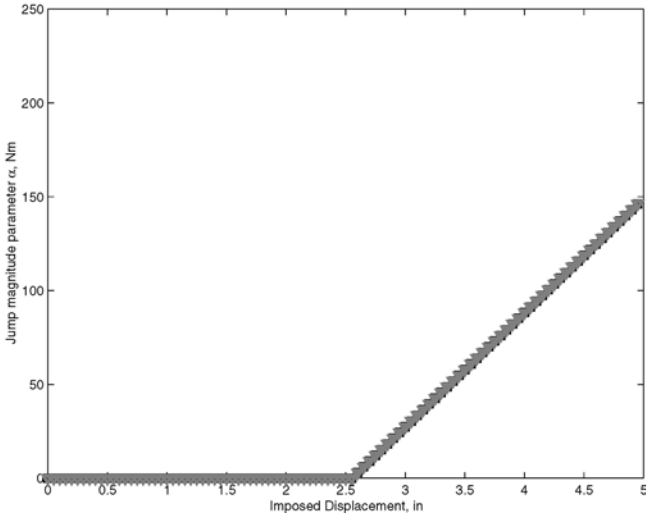

◀

Fig. 5.12 Push-over of a frame: equivalent plastic jump $\tilde{\alpha}$ versus imposed displacement $\bar{u}$. The hinges are numbered according to their initial onset. The diagram on the left top figure depicts the location of the hinges. The number of elements in the legend is the total number of elements in the frame model. All the plots follow the same legend

and

$$g_1(s) = 1 + 3\left(1 - \frac{2s_d}{h}\right)\left(1 - \frac{2s}{h}\right) \ , \tag{I.11}$$

as employed in (3.4).

Acknowledgements Financial support for this research has been provided by the ONR under grant no. N00014-00-1-0306 with UC Berkeley. This support is gratefully acknowledged.

References

Armero F (1999) Large-scale modeling of localized dissipative mechanisms in a local continuum: applications to the numerical simulation of strain localization in rate-dependent inelastic solids. Mech Cohesive-Frictional Mat 4: 101–131

Armero F (2001) On the characterization of localized solutions in inelastic solids: an analysis of wave propagation in a softening Bar. Comp Meth Appl Mech Eng 191: 181–213

Armero F, Ehrlich D (2002) An analysis of strain localization and wave propagation in plastic models of beams at failure. SEMM/UCB Report no. 2002/11, submitted to Comput Meth Appl Mech Eng

Armero F, Garikipati K (1995) Recent advances in the analysis and numerical simulation of strain localization in inelastic solids. In: Owen DRJ, Onate E, Hinton E (eds) Proceedings of COMPLAS IV, CIMNE, Barcelona.

Armero F, Garikipati K (1996) An analysis of strong discontinuities in multiplicative finite strain plasticity and their relation with the numerical simulation of strain localization in solids. Int J Solids and Structures, 33: 2863–2885

Attalla MR, Deierlein G, McGuire W (1994) Spread of plasticity: quasi-plastic-hinge approach. ASCE J Struct Eng 120, 2451–2473

Bažant Z, Belytschko T (1985) Wave propagation in a strain softening bar. ASCE J Eng Mech 111: 381–389

Bažant ZP, Cedolin L (1991) Stability of structures: elastic, inelastic, fracture and damage theories. Oxford University Press, New York

Bažant Z, Pan J, Pijaudier-Cabot G (1987) Softening in reinforced concrete beams and frames. ASCE J Struct Eng 113: 2333–2347

Bažant Z, Pijaudier-Cabot G, Pan J (1987) Ductility, snapback, size effect, and redistribution in softening beams of frames. ASCE J Struct Eng 113: 2348–2364

Crisfield MA (1984) Non-linear Finite Element Analysis of Solids and Structures. John Wiley & Sons, New York

Darvall PL (1984) Critical softening of hinges in portal frames. ASCE J Struct Eng 110: 157–162

Darvall PL, Mendis PA (1984) Elastic-plastic-softening analysis of plane frames. ASCE J Struct Eng 111: 871–887

Hughes TJR (1987) The Finite Element Method. Prentice-Hall, Englewood Cliffs, NJ

Jirásek M (1997) Analytical and numerical solutions for frames with softening hinges. ASCE J Eng Mech 123: 8–14

Jirásek M (2000) Comparative study of finite elements with embedded discontinuities. Comput Meth Appl Mech Eng 188: 307–330

King WS, White DW, Chen WF (1992) Second-order inelastic analysis of methods for steel-frame design. ASCE J Struct Eng 118: 408–428

Larsson R, Runesson K, Ottosen, NS (1993) Discontinuous displacement approximation for capturing plastic localization. Int J Numer Meth Eng 36: 2087–2105

Lubliner J (1990) Plasticity Theory. Macmillan Publishing Company, New York

Oliver J (1996a) Modelling strong discontinuities in solid mechanics via strain softening constitutive equations. Part 1: Fundamentals. Int J Num Meth Eng 39: 3575–3623

Oliver J (1996b) Modelling strong discontinuities in solid mechanics via strain softening constitutive equations. Part 2: Numerical Simulation. Int J Num Meth Eng 39: 3575–3623

Rots JG, Nauta P, Kusters G, Blaauwendraa T (1985) Smeared crack approach and fracture localization in concrete. Heron 30

Simo JC, Oliver J, Armero, F (1993) An analysis of strong discontinuities induced by softening solutions in rate independent solids. J. Comput Mech 12: 277–296

Spacone E, Filippou F, Taucer FF (1996a) Fiber beam-column model for nonlinear analysis of R/C Frames: Part I. Formulation. Earthquake Eng Struct Dyn 25: 711–725

Spacone E, Filippou F, Taucer FF (1996b) Fiber beam-column model for nonlinear analysis of R/C Frames: Part II. Applications. Earthquake Eng and Struct Dyn 25: 727–742